STATIC RESISTANCES OF COLD-FORMED HIGH STRENGTH STEEL TUBULAR NON-90˚ X-JOINTS

Madhup Pandey* and Ben Young

Department of Civil and Environmental Engineering, The Hong Kong Polytechnic University, Hong Kong, China

Abstract

This paper presents a test programme to investigate the static joint resistances and load vs deformation behaviour of cold-formed high strength steel (CFHSS) tubular non-90˚ X-joints. The investigation presented in this study predominantly focused on the chord failure of non-90˚ X-joints under brace axial compression loads. The experimental programme comprised of 26 tubular non-90˚ X-joints, which were fabricated with three included angles (θ_1), i.e. 30˚, 50˚ and 70˚. Circular and square hollow sections were used as braces, while chords were made up of rectangular and square hollow sections. The nominal yield strengths of the tubular members were 900 and 960 MPa. The brace and chord members were connected using automatic gas metal arc welding process. The measured value of brace-to-chord width ratio (β) ranged from 0.53 to 1, brace-to-chord thickness ratio (τ) ranged from 0.52 to 1.01, chord width-to-thickness ratio (2γ) ranged from 20.5 to 38.7 and chord side wall slenderness ratio (h_0/t_0) ranged from 15.4 to 38.9. A total of three failure modes was observed, including chord face failure, chord side wall failure and combination of these two failure modes. The static joint resistances obtained from the tests were compared with the nominal joint resistances of X-joints given in the CIDECT and Eurocode 3. It is shown that the existing design rules in these specifications are not suitable for the design of S900 and S960 steel grades tubular non-90˚ X-joints. Further, the impact of the included angle (θ_1) on the joint resistances of X-joints was observed by comparing the joint failure resistances of tubular non-90˚ X-joints obtained in this investigation with the joint failure resistances of tubular 90˚ X-joints of identical nominal tubular member dimensions and steel grades. In addition, tensile material properties from the weld heat affected regions of S960 steel grade tubular members of different thicknesses were also investigated.

Keywords: Experimental investigation; Non-90˚ X-joints; Rectangular hollow section joints; S900 and S960 steels; Thin-walled structures; Tubular connections.

*Corresponding author (e-mail: madhup.pandey@polyu.edu.hk)

1. Introduction

Cold-formed structural steels are popularly used in recent years in many structural applications around the globe. Latest technological advancements have allowed the production of cold-formed structural steels of different shapes and sizes. One of the popular shapes is the tubular section. The cold-formed steel tubular members are increasingly used as a primary structural member in various onshore and offshore structures, including bridges, high-rise buildings, large span roofs, truss girders, lattice structures, frameworks, offshore platforms and many more. The recent growth in metallurgical and automation sectors have caused a significant increase in the production of high strength steels (yield strength > 460 MPa). The high strength steel (HSS) hollow section members are now used in many construction projects owing to their high strength-to-weight ratios, improved toughness and good weldability compared to their traditional counterparts. It is due to these merits that the production of high strength structural steel complies with the requirements of sustainable development practice, which is now widely followed all around the world. It is the automobile sector, which is currently being benefitted by the HSS material, whereas the use of high strength structural steel is limited in the construction sector due to the lack of supporting research.

The research pertaining to the behaviour and design of rectangular and square hollow section (RHS and SHS) joints began around the mid-1960s mainly through theoretical and experimental studies. Afterwards, a significant amount of research was carried out under the flagship of the CIDECT and IIW in 1970s and 1980s, which led to the evolution of design rules for RHS joints. These design recommendations are mentioned in the guidelines and reports of the CIDECT [1] and IIW [2], and adopted by many international standards [3-7]. The design rules for tubular joints in the first editions of the CIDECT [8] and IIW [9] specifications were initially developed for those tubular sections which had dimensions and material properties (steel grades S355 or below) similar to the specimens used in the corresponding experimental programme [10]. In order to increase the applications of tubular members, the design rules in the first editions of the CIDECT [8] and IIW [9] were then extended up to the yield strength of 460 MPa in the latest editions of the CIDECT [1] and IIW [2]. A reduction factor (ζ) was applied on the joint resistance rules published in the first editions of the CIDECT [8] and IIW [9] in order to make them applicable for HSS grades.

In the literature, only a few studies dealing with the structural performance of CFHSS tubular joints with SHS and RHS chords are available. The static joint resistances of CFHSS – tubular T-joints, fully chord supported tubular T-joints and tubular X-joints were experimentally investigated by Pandey and Young [11-13]. The steel grades of hollow section members in these studies [11-13] were S900 and S960. The fully chord supported tubular T-joints are those T-joints

where the chord members of T-joints are fully supported along their entire length. Such structural applications can be seen in situations where the chord members of tubular T-joints are used to support the flooring systems. For instance, tubular T-joints supporting the floors of buildings, floors of tubular space frameworks, floors of tubular scaffolding, topside decks of offshore structures and many others. On the other hand, tubular X-joints are those tubular joints when the normal force component is transmitted through the chord member and is equilibrated by a brace member on the opposite side. The tubular X-joints can be seen at the intersection of wind bracings, bracings of truss bridges, at truss supports, in modified Warren truss and so on. Lan et al. [14] experimentally studied the performance of circular hollow section (CHS) T- and X-joints fabricated from Q960 steel plates. Feldmann et al. [15] conducted tests on K- and X-joints of RHS chords to assess the appropriateness of current reduction factors given in the CIDECT [1] and EC3 [3], where the nominal yield strengths of hollow section members were 500, 700 and 960 MPa. Havula et al. [16] tested T-joints with SHS chords fabricated from S420, S500 and S700 steels and subjected to brace in-plane bending. Thus, it can be noticed that there is no research available regarding the structural behaviour of CFHSS tubular non-90˚ X-joints. Hence, in this paper, efforts have been made to examine the joint resistances and load vs deformation behaviour of S900 and S960 steel grades tubular non-90˚ X-joints. The investigation presented in this study predominantly focused on the chord failure of non-90˚ X-joints under brace axial compression loads. The joint resistances obtained in this experimental investigation were compared with the nominal resistances calculated from the CIDECT [1] and EC3 [3]. Further, the impact of the included angle (θ_1) on the joint resistances of CFHSS X-joints was observed by comparing the joint failure resistances of tubular non-90˚ X-joints obtained in this investigation with the joint failure resistances of tubular 90˚ X-joints [13] of identical nominal tubular member dimensions and steel grades. Moreover, weld heat imparted on the parent metal during the course of welding operation has a significant influence on the overall joint behaviour, thus, the tensile material properties from the weld heat affected regions (WHAR) of CFHSS S960 steel tubular members of different thicknesses were also investigated in this study.

2. Test programme

2.1. Scope and general

The tests conducted in this study were designed to investigate the joint resistances and load vs deformation behaviour of CFHSS tubular non-90˚ X-joints. These joints were fabricated from CHS and SHS braces, while chords were made up of RHS and SHS members. The RHS (hereafter,

RHS includes SHS) and CHS used in this investigation were produced through the thermomechanical control process (TMCP). The steel grades of the tubular members used in this study were S900 and S960. In this test programme, two types of tubular non-90˚ X-joints were investigated, i.e., RHS-RHS and CHS-RHS. In the RHS-RHS configuration, RHS members were used as braces and chords. However, in the CHS-RHS configuration, CHS members were used as braces and RHS members were used as chords. Out of 26 tubular non-90˚ X-joints investigated in this experimental programme, 18 test specimens were made up of RHS-RHS configuration and 8 test specimens were made up of CHS-RHS configuration. The braces of tubular non-90˚ X-joints were subjected to incremental axial compression, while the chord members were not subjected to any external applied preload. As the HSS tubular members used in this investigation were seam-welded using high-frequency induction (HFI) welding, therefore, to examine the quality of seam-welds, all SHS chord members were such oriented that their seam-welds were located in their respective chord webs. In order to observe the effect of included angle (θ_1), a total of 3 sets of tubular non-90˚ X-joints, with identical nominal tubular member dimensions and steel grades, was fabricated in this experimental programme, wherein θ_1 was kept as 30˚, 50˚ and 70˚ for set-1, 2 and 3, respectively, as shown in Fig. 1. In this study, the brace and chord members of non-90˚ X-joints had identical nominal tubular member dimensions and steel grades as used by Pandey and Young [13] for tubular 90˚ X-joints.

2.2. Test specimens

The critical cross-sectional dimension ratios mainly affecting the static resistance of a tubular joint are brace width-to-chord width ratio ($\beta=b_1/b_0$), brace thickness-to-chord thickness ratio ($\tau=t_1/t_0$), chord width-to-chord thickness ratio ($2\gamma=b_0/t_0$) and chord side wall slenderness ratio (h_0/t_0). The test specimens were carefully designed to cover a wide range of these critical geometrical ratios in order to facilitate a comprehensive assessment of the applicability of the existing design provisions. In this study, the value of β ratio ranged from 0.53 to 1, τ ratio ranged from 0.52 to 1.01, 2γ ratio ranged from 20.5 to 38.7 and h_0/t_0 ratio ranged from 15.4 to 38.9. The definitions of symbols used to represent various dimensions of tubular non-90˚ X-joint are detailed in Fig. 2. Referring to Fig. 2, the overall cross-sectional width is represented by b, the overall cross-sectional depth is represented by h, the tube thickness is represented by t, outer corner radius is represented by R, inner corner radius is represented by r, brace or chord member length is represented by L and the angle contained between brace and chord is represented by θ_1. The subscripts 0 and 1 were respectively used to designate chord and brace members in this study. The overall flange widths (b_1 and b_0) and web heights (h_1 and h_0) of the SHS and RHS members, outside diameter (d_1) of the

CHS braces and the length of brace members at heel and toe locations (L_H and L_T) were measured using a two decimal place Mitutoyo digital calliper. The thicknesses (t_1 and t_0) were measured using a three decimal place Mitutoyo digital micrometre. The outer radii (R_1 and R_0) and inner radii (r_1 and r_0) were measured using Moore Wright radius gauges with a least count of 0.25 mm. The included angles at heel and toe locations (θ_H and θ_T) were measured using a digital spirit level.

For SHS braces, b_1 ranged from 80 to 120 mm, h_1 ranged from 80 to 120 mm and t_1 were 3 and 4 mm. For CHS braces, d_1 was 88.9 mm and t_1 were 3 and 4 mm. For RHS and SHS chords, b_0 ranged from 120 to 150 mm, t_0 ranged from 3 to 6 mm and h_0 ranged from 60 to 150 mm. The nominal chord length (L_0) was designed by taking a load distribution of 1 (vertical) to 1.5 (horizontal) from the intersection of brace and chord members at the heel location of tubular non-90˚ X-joint, as shown in Fig. 2. Thus, using simple geometry, the design formula for the nominal chord length (L_0) became $3h_0 + h_0 \tan(90\text{-}\theta_1) + h_1/\cos(90\text{-}\theta_1)$ where θ_1 was 30˚, 50˚ and 70˚ for set-1, 2 and 3, respectively. This nominal chord length (L_0) for tubular non-90˚ X-joint was designed by duly targeting that minimum length which can completely absorb the deformations of the chord member during the whole test duration so that the stresses at the brace and chord intersection could not be affected by the free chord ends. For brace members, the length at heel location (L_H) was kept equal to two times the maximum of b_1 and h_1 (i.e., $L_H = 2\max[b_1, h_1]$) for RHS and two times the brace diameter d_1 (i.e., $L_H = 2d_1$) for CHS. This designed brace length helped in averting the global buckling of the braces and overlapping of stresses between both ends of each brace member. Using simple geometry, the nominal design length of the brace member from the toe location (L_T) became equal to $L_H + h_1 \tan(90\text{-}\theta_1)$. The measured values of included angles at heel (θ_H) and toe (θ_T) locations, for all the three sets, are given in Tables 1 and 2 for RHS-RHS and CHS-RHS non-90˚ X-joints, respectively. The maximum deviations observed in the measured values of θ_H and θ_T were within ± 0.5˚. The positions of seam-welds in SHS chords were located in the chord web, while the positions of seam-welds in braces were facing the chord cross-section, as shown in Fig. 2. In this investigation, brace ends connecting braces to chord faces were wire-cut prior to their welding on to the chord faces using a high precision computer numerical controlled (CNC) wire-cutting machine, which ensured a uniform load transfer during the test. The measured average tubular member dimensions of RHS-RHS and CHS-RHS non-90˚ X-joints are respectively detailed in Tables 1 and 2. It is worth noting that every tubular member dimension of non-90˚ X-joints, as reported in Tables 1 and 2, was calculated by taking the mean of its respective 8 readings noted from different parts of that tubular member.

The nomenclature used for the labelling of test specimens was designed such that the joint type, nominal tubular dimensions of brace and chord members and the angle contained by them at

the heel location can easily be identified. In the labelling, the first letter means the joint type, which is X-joint, followed by the nominal brace dimensions represented by $d_1 \times t_1$ or $b_1 \times h_1 \times t_1$, chord dimensions represented by $b_0 \times h_0 \times t_0$ and the included angle (θ_1), all separated through the hyphen. In case the test was repeated with the identical test specimen, the letter "R" was then shown in the suffix of the label. As an example, the label X-100×100×4-120×60×4-30°-R represents a repeated X-joint with 100, 100 and 4 as the nominal cross-sectional width, depth and thickness of the brace; 120, 60 and 4 as the nominal cross-sectional width, depth and thickness of the chord; and an included angle of 30° between brace and chord members at heel location.

2.3. Material properties

In this study, CFHSS tubular members of 900MH and 960MH steel grades were used as the test material. The 900MH and 960MH steel grades tubular members were obtained by cold-forming of S900 and S960 steel grades plates followed by their high-frequency induction seam welding [17,18]. The material properties of 900MH and 960MH steel grades tubular members meet the requirements given in the EN [19]. The acronym 'MH' is based on the EN [19] designation for structural hollow sections, where 'M' stands for thermomechanically rolled steel (or, thermomechanical control processed steel) and 'H' stands for hollow section. In accordance with the mill reports, carbon equivalent values (CEV) of hollow section members ranged from 0.46-0.54, while carbon content ranged from 0.08-0.10%. In order to determine the material properties of hollow section members, longitudinal tensile and transverse compression coupons were extracted from different regions of tubular members. In order to minimise the heat generated during the cutting, the coupon specimens were fabricated using a high precision coolant based CNC wire-cutting machine, as discussed in Section 2.2 of this paper. The longitudinal tensile coupons were extracted from the flat, corner and curved regions of tubular members, as shown in Fig. 3. Following the recommendations given in the ASTM [20], the gauge width and gauge length of the flat coupons were 12.5 and 50 mm, respectively. However, for the corner and curved coupons, the gauge width and gauge length were 6 and 25 mm, respectively. In this study, the tubular non-90˚ X-joints were fabricated from the identical batch of tubes used by Pandey and Young [11] for the investigation of tubular 90° X-joints. The details regarding the tensile test-setup, test procedure and static tensile material properties are given in Pandey and Young [11].

In addition, from the flat regions of SHS and RHS chord side walls, compression coupons were extracted along the transverse direction of rolling. In this study, compression coupons of two sizes were fabricated, namely large size compression coupon and small size compression coupon. When the overall cross-sectional width (b_0) or depth (h_0) of SHS and RHS was less than 100 mm,

small size compression coupon of 26 mm length (transversely) and 13 mm width (longitudinally) was fabricated, whereas, for the other cases, large size compression coupon of 48 mm length (transversely) and 24 mm width (longitudinally) was fabricated. Before tests, the cross-sectional dimensions of coupons were carefully measured using Mitutoyo digital calliper, Mitutoyo digital micrometre and Mitutoyo point micrometre. These measured cross-sectional dimensions were used to calculate the actual cross-sectional areas of these coupons. A specially designed bracing jig was used for the compression coupon test. In this study, two sizes of bracing jigs were used, first, for the large size compression coupons, and second, for the small size compression coupons. The bracing jigs were specially designed to prevent the minor axis buckling of the compression coupons. The lengths and widths of the compression coupons were protruded by 1 mm from the bracing jig and from all the direction of the coupon specimen. After aligning the centre of the compression coupon with the centre of the bracing jig along both length and width direction, the bracing jig was then hand tightened. In order to record the strain measurements under compression, two linear Tokyo Measuring Instruments Laboratory (TML) strain gauges of type FLA-5-17-3L were attached at the mid-height on both edges of the compression coupon. Further, in order to avoid friction between the contact surfaces of the jig and compression coupon specimen, a thin layer of MOLYKOTE G-n metal assembly grease was used. Finally, the bracing jig was tight enough to avoid the buckling of compression coupon specimen along the minor axis, and at the same time, permitted unrestrained expansion due to the Poisson's effect.

Before the start of the compression coupon test, an initial preload of around 2 kN under load control mode was applied on the test specimen. The upper end of the testing machine was movable and could be adjusted to accommodate test specimens of different heights. A special ball-bearing was attached to this movable end. Under preload, the ball-bearing would adjust itself to ensure full contact with the upper end of the compression coupon test specimen, and thus, a uniform compression load was then transferred on the test specimen. The alignment and position of the test specimen were continuously adjusted until the discrepancies between the strain gauge readings were less than 5%. A displacement control mode was then used to drive the hydraulic and to apply axial compression loads on the compression coupon test specimens. The loading rates were 0.026 mm/min and 0.048 mm/min for the small and large size compression coupon test, respectively. Every compression coupon test was paused twice to prevent the effect of strain rate on the obtained material properties. Finally, static stress-strain curves were obtained from the test stress-strain curves using the load drops observed during the pause durations. The compression coupon test setup is shown in Fig. 4. The measured longitudinal tensile and transverse compression static material properties are summarised in Tables 3-6. The material properties include the initial Young's modulus (E_f, E_c, E_{cr} *and* E_{cp}), 0.2% proof strength ($\sigma_{0.2f}$, $\sigma_{0.2c}$, $\sigma_{0.2cr}$ and $\sigma_{0.2cp}$) which was

adopted as the yield strength, ultimate strength (σ_{uf}, σ_{uc} and σ_{ucr}) and fracture strain (ε_{ff}, ε_{fc} and ε_{fcr}). The sub-scripts *f*, *c*, *cr* and *cp* respectively stand for the flat, corner, curved and compression coupons. It should be stressed that these experimental material properties were obtained from their respective static stress-strain curves.

2.4. Welding

The welding of tubular non-90˚ X-joint test specimens was conducted through the gas metal arc welding (GMAW) process using a fully automatic welding robot controlled by certified and experienced welders. In order to protect the fresh weld deposits from the surrounding air, a gas mixture made up of 20% CO_2 and 80% Ar was purged during the welding process at the rate of 15-20 lit/min. In addition, during the welding operation, to avert the direct weld heat impact, the distance between the weld nozzle to parent metal was kept between 10 to 15 mm. Fig. 5 presents the photo of automatic GMAW of a tubular non-90˚ X-joint test specimen. The heat released during the welding process can significantly affect the resistance, and thus, the overall behaviour of tubular joints, therefore, it is imperative to carefully design the various welding process parameters. Pandey and Young [11] conducted various welding trials using different welding process parameters so as to obtain the aimed weld design by duly limiting the weld heat input. After various trials, the final selected value of the arc voltage (V) was 16 V, current (I) was 150 A and weld deposition speed (s) was 300 mm/min for the welding of tubular non-90˚ X-joint test specimens. It is worth noting that to prevent surplus weld heat input during the welding operation, and thus, to prevent excessive softening of the WHAR of test specimens, only a single weld pass was used in this study along with the minimum required weld leg size for all the test specimens The prequalified weld details of tubular joints in the CIDECT [1] and AWS [21] were used to design welds in this study. The filler material (i.e., welding wire) used in this study was made up of a low alloy solid carbon steel wire and conformed the ER120S-G class of the AWS [22]. The material properties of the filler material were obtained by conducting all-weld metal tensile coupon tests, as detailed in Pandey and Young [12]. For the filler material, the measured average values of yield strength, ultimate strength and fracture strain were 965.2 MPa, 1023.4 MPa and 17.2%, respectively [12]. The leg size of the fillet weld (FW) was denoted by w, the effective throat thickness of the FW was denoted by t_w, weld height for PJP groove weld (GW) was denoted by w' and its corresponding weld reinforcement was denoted by w_r. The measured average weld sizes at different locations, i.e., w, t_w, w' and w_r for the side welds, w_0 and t_w for the toe welds and w and t_w for the heel welds, are summarized in Tables 7 and 8 for RHS-RHS and CHS-RHS non-90˚ X-joint test specimens, respectively. The measured average weld sizes, as shown in Tables 7 and 8, were

obtained by taking the average of their respective 20 measurements. It should be noted that the connecting ends of the brace members at heel and toe locations were profiled as per the recommendations given in the CIDECT [1] for tubular non-90˚ joints. Furthermore, for the side welds, the outer edge of the connecting brace member end was bevelled at 45˚ in order to obtain a prequalified PJP groove weld profile, which is in accordance with the AWS [21]. The side, toe and heel locations of a tubular non-90˚ X-joint are shown in Fig. 2, while the typical weld profiles used at these locations are shown in Fig. 6. For equal-width joints (β=1), the values of root gap (G) between brace and chord members were calculated using the expression proposed by Teh and Rasmussen [23], as shown below:

$$G = \sqrt{(R_0 + g)^2 + (R_0 - t_1)^2} - R_0 \quad (1)$$

In this experimental programme, the brace and chord members of all the equal-width (β=1) tubular non-90˚ X-joints were tack welded without keeping any spacing between them (i.e., g=0). Therefore, using Eq. (1), the calculated values of the root gap (G) for all the RHS-RHS equal-width (β=1) tubular non-90˚ X-joints are detailed in Table 7. From Table 7, it can be noted that the values of the root gap (G) for all the RHS-RHS equal-width (β=1) tubular non-90˚ X-joints are less than 3 mm, which is the upper limit mentioned in the CIDECT [24].

2.5. Weld heat affected region (WHAR) investigation

2.5.1. General

The HSS available in the market are mainly produced by quenched and tempered (QT) and TMCP manufacturing processes. It should be noted that the latest editions of international standards do not differentiate HSS by the production process. However, HSS produced via different production processes possessed different chemical composition and microstructure, and thus, they behave differently under welding [25]. The main factors affecting the post-weld microstructure and WHAR material properties include welding process parameters (current, voltage and weld deposition speed), chemical composition of the parent material, welding type and cooling rate. Due to the large heat released during the welding process, the original phase and microstructure of the parent material get changed. The most severe WHAR during the welding is the region where the weld metal gets fused with the parent metal (i.e., the fusion zone, FZ) followed by the immediate region surrounding the freshly deposited weld material (i.e., the heat affected zone, HAZ). The HSS produced using TMCP have relatively lower carbon equivalents compared to similar quenched HSS. Consequently, TMCP steels can be welded at lower pre-heat temperature using the identical welding operation parameters [26]. Moreover, the original microstructure of TMCP steel, and thus,

its material properties are due to the low-temperature thermo-rolling process. Owing to high weld heat energy, the original microstructure and the outcome of the heat treatment process in TMCP steel get lost. Stroetmann et al. [25] discovered a relatively higher strength reduction in the HAZ of TMCP HSS compared to quenched HSS. Javidan et al. [27] observed around 30% strength reduction in the HAZ region of TMCP tubular members made up of S960 steel. Therefore, during the welding process, TMCP HSS needs careful attention so as to avoid the unwanted softening of the WHAR.

2.5.2. Tensile coupon test specimens from WHAR

In order to determine the material properties from the HAZ of S960 steel grade TMCP tubular members, three CFHSS WHAR tubular test specimens of different thicknesses (t=3, 4 and 6 mm) were fabricated in this study, as shown in Fig. 7. The tubular members were welded using the automatic GMAW process. The details pertaining to welding fabrication procedures, weld design, filler material and welding process parameters were kept identical to the welding of tubular non-90˚ X-joint test specimens, as mentioned in Section 2.4 of this paper. It should be noted that the tubular members investigated in this study were not subjected to any pre-heating before the welding process due to the small thicknesses ($t \leq 6$ mm) of the parent metals. After welding, the tubular test specimens were then allowed to cool down naturally under ambient temperature conditions. Subsequently, from the first 24 mm distance from the fillet weld toe of these CFHSS WHAR tubular test specimens, tensile coupon specimens of sub-size dimensions were extracted. The gauge width of the sub-size coupon was 6 mm, while its associated gauge length was 25 mm. The subsize coupon dimensions given in the AWS [20] were selected so as to obtain the material properties as close as possible in the HAZ. Further, for comparison, a tensile coupon of identical dimension was also extracted from the non-HAZ (i.e., parent metal) region. It should be noted that the brace and chord members of each WHAR tubular test specimen, as shown in Figs. 7(a), 7(b) and 7(c), were taken from the same tube. Thus, brace and chord members of each WHAR tubular test specimen possessed identical thickness, cross-sectional dimensions, steel grade and belonged to the identical batch of tubes. Therefore, when the chord members of WHAR tubular test specimens were short in length (i.e., for test specimens with 3 and 4 mm thicknesses), the coupon specimens from the HAZ and non-HAZ regions were extracted from its brace member. Hence, in this study, the WHAR tensile coupon specimens of 3 and 4 mm thicknesses were extracted from the brace member, while WHAR coupon specimens of 6 mm thickness were extracted from the chord member. These tensile WHAR coupons were fabricated along the transverse direction of the cold-rolling and from the flat regions of the tubular members. In order to reduce the heat generated during the fabrication of these

coupon specimens, coolant based high precision CNC wire-cutting machine was used. Fig. 8 presents a representative photo showing the extracted location of HAZ tensile coupons in the brace and chord members, whereas Fig. 9 presents the photo of extracted tensile coupon test specimens from the HAZ and non-HAZ regions. The test setup and test procedure for the tensile tests of HAZ and non-HAZ coupon specimens were similar to the details given in Section 2.3 of this paper.

2.5.3. Test results and discussions

The experimentally obtained static stress-strain curves corresponding to the HAZ and non-HAZ regions of 3, 4 and 6 mm thicknesses are shown in Figs. 10, 11 and 12, respectively. Table 9 presents the measured material properties calculated from these curves. The residual factors obtained by normalising the HAZ material properties with their corresponding non-HAZ material properties are detailed in Table 10. From Table 10, it can be noticed that the ultimate strengths of tensile coupons extracted from S960 steel grade TMCP tubular members of thicknesses 3, 4 and 6 mm were reduced as much as by 32%, 25% and 14% in their first 6 mm regions from the weld toe, respectively. This reduction in the ultimate strength was due to the softening of the WHAR as a result of weld heat input. The curves presenting the variations of residual factors of Young's modulus, yield strength (i.e., 0.2% proof stress), ultimate strength and fracture strain from the HAZ of different investigated thicknesses are shown in Fig. 13. The residual initial Young's modulus, across the entire HAZ, retained more than 90% of its values obtained for the virgin parent metal, as shown in Fig. 13(a). The variations of yield strength residual factor with distance from the weld toe are presented in Fig. 13(b). It is evident from previous studies [28-30] that the shape of stress-strain curves changes with the increase of temperature. As the yield strength, in this study, was determined using the slope of initial Young's modulus at 0.2% strain, therefore, the yield strengths of HAZ tensile coupons change with change in the slope of the initial part of the stress-strain curves. The variations of ultimate strength residual factors with distance from the weld toe are presented in Fig. 13(c). The deterioration in the strengths of virgin parent metals of different thicknesses can be best visualised from the variations of residual ultimate strength with distance from the weld toe. It can clearly be noticed that the ultimate strength in the HAZ increased with the increase of distance from the weld toe. In addition, the deterioration is more serious for thin-walled tubular members compared to thick-walled tubular members. The variations of fracture strain residual factor with distance from the weld toe are presented in Fig. 13(d). The fracture strain of weld heat exposed specimens mainly depends on the thickness of the specimen and weld heat exposure temperature. The specimen with a small thickness and large weld heat exposure possessed very ductile fracture due to excessive softening of the parent metal. In addition, specimens with small thicknesses were

more sensitive towards the weld heat exposure and possessed a large scatter compared to the thick specimen.

It should be noted that the temperature distribution per unit length, in the WHAR, is highly non-linear along the perpendicular direction of the weld toe edge. The behaviour of different WHAR mainly depends on the range of weld heat exposure temperature with respect to the A_{C1} and A_{C3} temperatures of the parent metal. During the heating process, when austenite started to form in the steel material, then that particular temperature is termed as its A_{C1} temperature. Whereas, during heating, when the transformation to austenite from ferrite is completed, then that particular temperature of steel is termed as its A_{C3} temperature. Depending on whether the weld heat exposure temperature is less than A_{C1} or between A_{C1} and A_{C3} or higher than A_{C3}, the weld heat exposed steel transformed to different phases of steels. If the weld heat exposure temperature is below the A_{C1} temperature of the parent metal, a mild growth of ferrite grains will occur, and thus, leads to a minor reduction in the strength of the parent metal. When the local weld heat exposure temperature is in between A_{C1} and A_{C3}, the replacement of ferrite grains with austenite grains would occur. However, once the local weld heat exposure temperature exceeds A_{C3}, all ferrite grains would be replaced by the austenite grains. In addition, it is essential to note that the rate of cooling after the welding operation has an important influence on the material properties of the WHAR. As the temperature distribution in the WHAR is non-linear, thus, different WHAR cooled down with different cooling rates. When the WHAR cooled down within a very short duration, cold cracks could appear due to excessive hardening. Thus, the stress-strain curve of a particular region of the WHAR could be very different compared to its adjacent region and directly depends on its local weld heat exposure temperature and post-welding cooling rate. It is noteworthy to mention that the HAZ strength reductions obtained in this investigation are only limited for S960 steel grade TMCP tubular members welded by automatic GMAW process with specific welding process parameters, as detailed in Section 2.4. It is expected that the experimental outcomes would vary depending on the type of steel, steel grade, steel manufacturing method, welding process type, welding operation parameters, number of weld passes, weld shape and weld size.

2.6. Non-90˚ X-joint test setup

Axial compression tests on tubular non-90˚ X-joints were conducted in 1000 and 5000 kN servo-controlled hydraulic testing machines. Except for X-120×120×4-120×120×4-30˚ and X-88.9×4-120×120×6-30˚ test specimens, all other tests were conducted in the 1000 kN testing machine, whereas, due to capacity concerns, only these two tubular non-90˚ X-joints were tested in the 5000 kN testing machine. A 0.3 mm/min displacement control rate was used to apply axial

compression loads on all the test specimens. The schematic sketch of the tubular non-90˚ X-joint test setup is shown in Fig. 14. The top supports of both the testing machines were adjustable so that the non-90˚ X-joint test specimens with different overall heights could easily be tested. A specially designed spherical ball-bearing was pre-bolted on the top support of the test rig. This specially designed spherical ball-bearing could easily adjust itself during the initial load transfer to the top brace end. In order to confirm complete contact with the end of the top brace member, a solid steel plate was pre-attached on the ball-bearing, which in turn eliminated any gaps between the top solid steel plate and top brace end during the load transfer. On the bottom side of the test specimen, a solid steel block was placed on the solid rigid support, which in turn was bolted to the actuator ram of the test rig.

Before the start of the test, the specially designed spherical ball-bearing was unlocked and could freely rotate in any direction. The tubular non-90˚ X-joint test specimen was seated on the bottom solid steel block after being carefully aligned along both the longitudinal and transverse direction of the test rig. The movable ram of the test machine was slowly ramped up by duly keeping the top support fixed until approximately 2 to 3 mm gap was left between the top brace member and the top support of the testing machine. A 0.1 kN/sec load-control rate was used to close this gap. During this closure, the specially designed spherical ball-bearing undertook a fixed position as per the cutting profile of the top brace end. Subsequently, for the remaining test, the ball-bearing was then fixed at this position to prevent its further rotation in any direction. Due to this locking, the ball-bearing could not rotate in any direction. Thus, the support conditions at the top and bottom brace ends can now be considered as fixed ends, thus only axial load can be applied on the test specimen without allowing major and minor axis rotations. This meticulous test procedure helped to apply pure axial compression load on the test specimens. Figs. 15 and 16 respectively present the photos of tubular non-90˚ X-joint test setups for the 1000 kN and 5000 kN testing machine used in this investigation. During tests of all non-90˚ X-joint test specimens, various deformations, including overall axial shortening of the test specimen, chord face indentations and chord side wall deformations, were carefully measured using pre-calibrated linear variable displacement transducers (LVDTs). In this study, indentations at toe locations of both faces of the chord member were measured by two methods, first, by measuring indentations along the direction of the applied axial compression load (LVDT-2 and 5), and second, by measuring indentations perpendicular to the chord connecting faces (LVDT-3 and 6). On the other hand, due to space limitation at the heel locations, the chord face indentations were measured only along the direction of the applied axial compression loads (LVDT-1 and 4). The indentations at both toe and heel locations of chord connecting faces were recorded via extended LVDT arms. In order to measure the actual indentation, the bases of LVDTs (LVDT-1 to 6) were placed on the chord faces.

Due to this positioning of LVDTs, the measured values of chord face indentations excluded the contributions due to the vertical shortenings of the chord side walls. It is worthy to note that the contribution of the vertical shortenings of the chord side walls increased with the increase of β ratio. Thus, it was imperative to adopt a correct approach for the actual measurement of the chord face indentations.

The chord side wall deformations were measured for both webs of the chord, using LVDTs with Poly Methyl Methacrylate plates connected at their tips (LVDT-7 and 8). As the exact location of the maximum chord side wall deformation was difficult to predict, thus, the use of Poly Methyl Methacrylate plates facilitated in locating the actual maximum chord side wall deformation. Two lateral LVDTs (i.e., one for each chord web; LVDT-7 and 8) were used when the included angles (θ_H) of the test specimens were 50˚ and 70˚, whereas four lateral LVDTs (i.e. two for each chord web; LVDT-7a, 7b, 8a and 8b) were used when the included angles (θ_H) of test specimens were 30˚. The reason for using four lateral LVDTs (LVDT-7a, 7b, 8a and 8b) for test specimens with θ_H=30˚ was due to the presence of a relatively large chord side wall region between the brace members. In addition, two pre-calibrated inclinometers (i.e., one on each side of the brace members; inclinometer-11 and 12) were also attached precisely at the base locations of LVDTs, which were used to measure the chord face indentations. The in-plane rotation of the chord member was measured with the help of these two inclinometers (inclinometer-11 and 12). Moreover, the upward movement of the actuator ram was measured with the help of LVDTs placed at the diagonal ends of the actuator ram (LVDT-9 and 10). After pre-loading, the rest of the test was continued using the displacement control loading so as to obtain the test results also in the post-ultimate region. Furthermore, the impact of loading rate from the obtained joint resistances was averted by pausing the test twice for 120 seconds. Therefore, using the load drops obtained by pausing the tests, test load vs deformation curves were converted into static load vs deformation curves. With the help of an advanced data acquisition logger, the values of applied axial compression loads and LVDT measurements were carefully recorded at a regular interval of time. In this study, for all test specimens, trivial chord-in-plane rotation was observed. For example, Fig. 17 presents the chord-in-plane rotations of the test specimens X-120×120×4-120×120×4-30° and X-120×120×3-150×150×6-50°.

2.7. Test results

The results obtained from the tests of tubular non-90˚ X-joint test specimens are presented in terms of load vs deformation curves, including load vs chord face indentation curves measured at both heel and toe locations and load vs chord side wall deformation curves, as shown in Figs. 18-21.

It is worth noting that the load vs deformation curves, shown in Figs. 18-21, are static curves, which in turn were obtained from their corresponding test curves. The joint resistance of test specimens, in this study, was determined in accordance with the recommendations given in the CIDECT [1], where the joint failure resistance was taken as the resistance corresponding to the first occurrence of either ultimate deformation limit load or ultimate load, which was also used by Pandey and Young [11-13]. The recommendation laid out in the CIDECT [1] regarding the ultimate deformation failure load criterion was adopted in this study, where the load corresponding to $0.03b_0$ chord face indentation was taken as the failure load. In order to obtain conservative joint resistances for all non-90˚ X-joint test specimens, out of various LVDTs measuring chord face indentations, the load vs chord face indentation curves corresponding to maximum chord face indentation location was selected to determine the joint failure resistance. In this investigation, the maximum chord face indentations were observed at the toe locations (LVDT-2 and 5) of all tubular non-90˚ X-joint test specimens. On the other hand, the chord face indentations measured at the heel locations (LVDT-1 and 4) of tubular non-90˚ X-joints were very trivial (or ignorable) and mainly composed of vertical slips of LVDT stroke. It is worth noting that for all tubular non-90˚ X-joint test specimens, the measured values of chord face indentations were always greater when recoded along the direction of the applied loads (LVDT-2 and 5) in contrast to the measurements recorded perpendicular to the chord connecting faces (LVDT-3 and 6). Therefore, the load vs chord face indentation curves and subsequent data analyses and joint resistance calculations were all based on the chord face indentations measured along the direction of the applied brace axial compression load (LVDT-2 and 5). Thus, the absence of chord face perpendicular LVDTs at the heel locations of tubular non-90˚ X-joints had no effects on the joint resistance determination. Similarly, the load vs chord side wall deformation curve was based on the chord web with maximum chord side wall deformation. Fig. 22 graphically presents the definition of joint failure resistance adopted in this investigation. In Fig. 22(b) and Tables 11-13, N_{max} represents ultimate joint resistance of tubular non-90˚ X-joint, $N_{3\%}$ represents the joint resistance corresponding to the ultimate deformation limit criterion and $N_{f,\theta 1}$ represents joint failure resistance corresponding to the first occurrence of N_{max} and $N_{3\%}$. For those tubular non-90˚ X-joints where no ultimate load (or peak load) was noticed and the load vs deformation curves were continuously increasing, the maximum test loads (N_{max}) for such test specimens were not applicable (N.A.), and thus, not reported in Tables 11 and 13. In addition, Fig. 23 presents the definition of $0.03b_0$ deformation limit and its relationship with the LVDTs measuring the chord face indentation (u). In order to check the reliability levels of test results, repeated tests were conducted for X-100×100×4-120×60×4-30˚, X-88.9×4-120×120×6-50˚ and X-88.9×3-120×60×4-70˚. The joint failure resistances of X-100×100×4-120×60×4-30˚-R, X-88.9×4-120×120×6-50˚-R and X-88.9×3-120×60×4-70˚-R repeated tests differed from their

corresponding original tests by 3.36%, 3.49% and 1.89%, respectively. The small differences in the joint failure resistances of these non-90˚ X-joints affirmed the accuracy of the test results obtained in this experimental programme. It should be stressed that, during the tests, no cracks were observed at the chord seam-weld, chord corner and brace-chord intersection regions.

2.8. Discussion of results

On observing the load vs deformation curves, as shown in Figs. 18-21, it can be noticed that the RHS-RHS non-90˚ X-joints with β=0.53 possessed no clear ultimate load, where the applied load was continuously increasing with the increase of the chord face indentation deformation. In addition, the post-yield stiffness, which is represented by the slope of load vs deformation curve after the yielding of the chord connecting face, of RHS-RHS non-90˚ X-joints with small β ratio (β < 0.60) decreased with the increase of the chord face indentation deformation. For such non-90˚ X-joints, due to the minimal out-of-plane stiffness of the chord connecting face, the top and bottom chord connecting faces possessed membrane action when subjected to brace axial compression loads. Hence, due to the membrane action of the chord connecting face and strain hardening of the material, the load vs deformation curves were continuously increasing with the increase of the applied load. The RHS-RHS equal-width non-90˚ X-joints (β=1.0) possessed an evident ultimate load in their load vs deformation curves and the joint failure resistances of all such joints were load controlled. For such joints, the axial compression load applied through the brace members were mainly resisted by the chord side walls. Therefore, due to the buckling of chord side walls under the applied axial compression load, the equal-width RHS-RHS non-90˚ X-joints possessed a clear ultimate (or peak) load in the load vs deformation curves, as shown in Fig. 20. Further, for RHS-RHS equal-width non-90˚ X-joints, the applied loads dropped gradually in their post-ultimate regions. It is important to note that for all RHS-RHS equal-width non-90˚ X-joints, the load vs chord face indentation curves at heel locations (LVDT-1 and 4) were entirely composed of the slips of LVDT stroke, as no chord face indentations were noticed at the heel locations of these joints. Therefore, the load vs chord face indentation curves at the heel locations of RHS-RHS equal-width non-90˚ X-joints are not presented in this paper. With regard to RHS-RHS non-90˚ X-joint test specimens having β = 0.80, 0.84 and 0.86, ultimate loads can be seen in their corresponding load vs deformation curves. Further, for all these joints, the joint failure resistances were load controlled, as the ultimate loads occurred before their corresponding deformation limit loads. For RHS-RHS non-90˚ X-joints with large β ratio ($0.80 \leq \beta < 1.0$), the side walls of brace members were positioned near the chord corner regions. The out-of-plane stiffness of the chord corner regions was relatively large than the out-of-plane stiffness of the corresponding chord central region.

Consequently, the applied axial compression load through the brace members was partially transferred to the chord connecting face and partially transferred to the chord side walls. Unlike RHS-RHS non-90˚ X-joints with small β ratio, membrane action of the chord connecting faces would be very small for RHS-RHS non-90˚ X-joints with large β ratio. Hence, due to these reasons, the load vs deformation curves of RHS-RHS non-90˚ X-joints with large β ratio possessed gradual ultimate loads at large values of chord face indentations.

As shown in Fig. 21, for CHS-RHS non-90˚ X-joints with brace thickness equal to 4 mm, the attainment of ultimate load and the corresponding post-ultimate load drop in their respective load vs deformation curves were very gradual. Whereas, for test specimens with brace thickness equal to 3 mm, the load vs deformation curves showed no clear ultimate loads. In general, compared to RHS-RHS non-90˚ X-joints, the CHS-RHS non-90˚ X-joints showed improved deformation capacity. The load vs deformation curves of all CHS-RHS non-90˚ X-joint test specimens showed a nearly stagnant phase at large values of chord face indentations, thus, the joint failure resistances ($N_{f,\theta 1}$) of these test specimens were deformation controlled. From the obtained test results, it is noted that on increasing the included angle (θ_1) from 30° to 50°, the joint failure resistances ($N_{f,\theta 1}$) of tubular non-90˚ X-joints dropped by an average of 38.5%. However, on increasing the included angle (θ_1) from 30° to 70°, the joint failure resistances ($N_{f,\theta 1}$) of tubular non-90˚ X-joints dropped by an average of 48.9%. Also, on increasing the value of included angle (θ_1), the initial stiffness, joint resistance and post-yield stiffness of tubular non-90˚ X-joints reduced. These reductions are more serious during the initial increase of the included angle (θ_1). With the increase of included angle (θ_1), test specimens possessed a shorten elastic response and gradual yielding transition compared to the test specimens with θ_1=30˚. For test specimens with large values of included angle (θ_1=50˚ and 70˚), the attainment of ultimate load and corresponding post-ultimate load drop was relatively more gradual compared to the test specimens with the small value of included angle (θ_1=30˚).

2.9. Failure modes

For RHS X-joints, typical failure modes are elaborately mentioned in the CIDECT [1] and EC3 [3]. For tubular non-90˚ X-joints, the effect of chord shear transferred through the flanges and webs of the chord members came into effect. This effect was more dominating for test specimens with small values of included angle (θ_1). Three failure modes were observed in this investigation, which includes chord face failure (F), chord side wall failure (S) and their combination (F+S). The after test photos of test specimens which failed in these failure modes are shown in Figs. 24 and 25 for RHS-RHS and CHS-RHS non-90˚ X-joints, respectively. The flanges and webs of chord

members undergone a considerable plastic deformation in all the observed failure modes. For most of the test specimens, no overall and local buckling was observed in the brace members. However, for X-120×120×3-150×150×6-50˚ and X-120×120×3-150×150×6-70˚, local buckling occurred in brace members near the brace-chord connection region soon after the ultimate loads of these joints. In this study, the chord face failure (F) mode was defined as the mode when the joint failure resistance of that joint was only controlled by its chord face indentation limit. The test specimens that failed in 'F' mode had shown no ultimate loads in their respective load vs chord face indentation curves. Also, in 'F' mode, it was observed that most of the deformations were contained in the flat regions of the chord connecting faces with marginal participation of the corresponding chord corner regions. On the other hand, the chord side wall failure (S) mode was defined for equal-width tubular non-90˚ X-joints (β=1), as the applied loads in these joints were predominantly resisted by the chord side walls. This definition of chord side wall failure (S) mode of equal-width RHS-RHS non-90˚ X-joints is in-line with the current recommendations given in the CIDECT [1] and EC3 [3]. In this study, the joint failure resistances ($N_{f,\theta 1}$) of equal-width RHS-RHS non-90˚ X-joints were entirely strength controlled. Moreover, in this investigation, a combined failure mode (F+S) was introduced for test specimen having $\beta \neq 1$ and also possessed ultimate load in its respective load vs deformation curve. The joint failure resistances ($N_{f,\theta 1}$) of such test specimens were jointly controlled by ultimate load and $0.03b_0$ indentation criteria. This failure mode was characterised by the combined deformations of the chord face, chord corner regions and chord side walls. Tables 14 and 15 present the observed failure modes, measured values of chord face indentation (u) and the chord side wall deformation (v) at the failure loads and the governing deformation, out of u and v, at failure loads for RHS-RHS and CHS-RHS non-90˚ X-joints, respectively. In addition, it should be stressed that the proposed limits of β values corresponding to the observed failure modes of RHS-RHS and CHS-RHS non-90˚ X-joints are only restricted for this study. In order to propose the general limits of β ratio for the observed failure modes of CFHSS RHS-RHS and CHS-RHS non-90˚ X-joints, a detailed parametric study, possibly through numerical investigation, is required. The coverage of this paper is only limited to the experimental investigation of CFHSS RHS-RHS and CHS-RHS non-90˚ X-joints of S900 and S960 steel grades.

3. Reliability analysis

Using the guidelines of the AISI S100 [31], a reliability analysis was conducted to evaluate the reliability of the design rules given in the CIDECT [1] and EC3 [3]. The equation used to calculate the reliability index (β_0) can be obtained from Pandey and Young [11]. For the calculation of the reliability index (β_0), the values M_m, F_m, V_M, V_F and V_Q were taken as 1.10, 1.0, 0.10, 0.10

and 0.21, respectively. In order to evaluate the design rules given in the EC3 [3], a load combination of 1.35DL+1.5LL was used in accordance with the EC [32]. However, for the reliability evaluation of the design rules given in the CIDECT [1], a load combination of 1.2DL+1.6LL was used in accordance with the ASCE 7 [33]. In this paper, the design rules were considered reliable when $\beta_0 \geq 2.5$.

4. Existing design rules

4.1. General

The comparisons of joint failure resistances ($N_{f,\theta 1}$) obtained from tests with the nominal resistances ($N^*_{C,X}$, $N_{C,X}$, $N^*_{E,X}$ and $N_{E,X}$) of the CIDECT [1] and EC3 [3] are presented in Tables 11-13 for the observed failure modes of RHS-RHS and CHS-RHS non-90° X-joints. The design rules of tubular X-joints in the CIDECT [1] and EC3 [3] fundamentally differ in the definitions of HSS reduction factor (ζ), partial safety factor (γ_M) and design yield strength (f_{yd}). The partial safety factors associated with the observed failure modes of X-joints were used to convert design resistances into nominal resistances. The nominal resistances of non-90° X-joints given in the CIDECT [1] and EC3 [3] were calculated by two approaches, i.e., by with and without incorporating the recommended reduction factors. When reduction factors were not incorporated then the nominal resistances calculated from the CIDECT [1] and EC3 [3] were denoted by $N^*_{C,X}$ and $N^*_{E,X}$, respectively. However, when reduction factors were incorporated, then the nominal resistances calculated from the CIDECT [1] and EC3 [3] were denoted by $N_{C,X}$ and $N_{E,X}$, respectively. These two approaches were adopted to evaluate the appropriateness of both previous (for mild steel) and current design rules of the CIDECT [1] and EC3 [3]. The nominal resistances were obtained using the measured tubular member dimensions, as shown in Tables 1 and 2, and experimentally obtained material properties [11]. It should be noted that both the CIDECT [1] and EC3 [3] recommend a direct interpolation between joint resistances at β=0.85 and 1.0, when $0.85 < \beta < 1$. Furthermore, when a joint has CHS braces connected to RHS chord, both the CIDECT [1] and EC3 [3] recommend replacing b_1 by d_1 and multiplying the design rules by $\pi/4$.

4.2. EC3 design provisions

The design rules for tubular joints in the EC3 [3] are valid for tubular members with yield strengths up to 460 MPa. Using the EC3 [34], the design provisions of the EC3 [3] were extended up to 700 MPa by multiplying the original design rules with the reduction factors. When the yield

strength of tubular member falls between 355 to 460 MPa (i.e. 355 < $f_y \leq 460$), 0.9 should be used as a reduction factor. However, when the yield strength of tubular member falls between 460 to 700 MPa (i.e. 460 < $f_y \leq 700$), 0.8 should be used as a reduction factor. The design yield strength for tubular joints in the EC3 [3] is defined as the actual yield strength of the tubular member and taken as 0.2% proof stress in this study. Therefore, the measured 0.2% proof stresses were used to calculate the nominal resistances from the EC3 [3]. Moreover, the value of the partial safety factor for tubular joints (γ_{M5}) in the EC3 [3] was equal to 1.0 for all types of failure modes and tubular joint configurations. The design rules for chord face failure and chord side wall buckling modes, without and with incorporating the reduction factors, are as follows:

Chord face failure ($\beta \leq 0.85$)

when reduction factor is not incorporated:

$$N_{E,X}^{*} = \frac{k_n f_{y0} t_0^2}{(1-\beta)\sin\theta_1}\left(\frac{2\eta}{\sin\theta_1} + 4\sqrt{1-\beta}\right) / \gamma_{M5} \tag{2}$$

when reduction factor is incorporated:

$$N_{E,X} = \zeta\left[\frac{k_n f_{y0} t_0^2}{(1-\beta)\sin\theta_1}\left(\frac{2\eta}{\sin\theta_1} + 4\sqrt{1-\beta}\right) / \gamma_{M5}\right] \tag{3}$$

Chord side wall buckling (β=1)

when reduction factor is not incorporated:

$$N_{E,X}^{*} = \frac{k_n f_b t_0}{\sin\theta_1}\left(\frac{2h_1}{\sin\theta_1} + 10t_0\right) / \gamma_{M5} \tag{4}$$

when reduction factor is incorporated:

$$N_{E,X} = \zeta\left[\frac{k_n f_b t_0}{\sin\theta_1}\left(\frac{2h_1}{\sin\theta_1} + 10t_0\right) / \gamma_{M5}\right] \tag{5}$$

In Eqs. (2)-(5), k_n is the chord stress function that accounts for the effect of external chord stresses on the joint resistance. In this study, as no external force was applied on the chord members, thus, k_n was taken as unity in this study. In Eqs. (4) and (5), the chord side wall buckling strength (f_b) was based on the buckling curve "c" for cold-formed hollow sections, as per EC3 [35]. The definitions of other terms used in Eqs. (2)-(5) are already explained in the previous sections of this paper.

4.3. CIDECT design provisions

The design rules for tubular joints in the CIDECT [1] are valid for tubular members with yield strengths up to 460 MPa. However, when the yield strength of the tubular member exceeds

355 MPa (i.e. f_y > 355), 0.9 should be used as a reduction factor. Unlike the definition of design yield strength in the EC3 [3], the minimum of – the yield strength and 80% of the ultimate strength – was taken as the design yield strength in the CIDECT [1]. From Table 3, it can be noticed that for all the tubular members, 80% of the ultimate strengths were always lower than their corresponding 0.2% proof stresses. Therefore, the measured 80% of the ultimate strengths were used to calculate the nominal resistances for the comparisons. The partial safety factors are not explicitly mentioned in the design equations of the CIDECT [1], however, their effects have already been incorporated inside the design equations [1]. In this study, the nominal resistances from the CIDECT [1] were obtained by using the partial safety factors (γ_M) of 1.0 for chord face failure and 1.25 for chord side wall failure modes. For joints with β ratio ranging between 0.85 to 1, chord punching shear may become critical. Thus, in order to obtain the nominal resistances corresponding to chord punching shear failure, γ_M equal to 1.25 associated with the effective width of punching shear ($b_{e,p}$) was used in this study. It should be noted that the values of partial safety factors are given in annex C of the IIW [2] for different joint types and their corresponding different failure modes. For more details regarding the adoption of partial safety factors for tubular joints, reference can be made to Wardenier [36] and Pandey and Young [11,13]. The design rules for chord face plastification and chord side wall failure modes, with and without incorporating the reduction factors, are as follows:

Chord face plastification ($\beta \leq 0.85$)

when reduction factor is not incorporated:

$$N_{C,X}^{*} = Q_f \frac{f_{y0} t_0^2}{\sin\theta_1}\left(\frac{2\eta}{(1-\beta)\sin\theta_1} + \frac{4}{\sqrt{1-\beta}}\right) \tag{6}$$

when reduction factor is incorporated:

$$N_{C,X} = \zeta\left[Q_f \frac{f_{y0} t_0^2}{\sin\theta_1}\left(\frac{2\eta}{(1-\beta)\sin\theta_1} + \frac{4}{\sqrt{1-\beta}}\right)\right] \tag{7}$$

Chord side wall failure (β=1)

when reduction factor is not incorporated:

$$N_{C,X}^{*} = Q_f \frac{f_k t_0}{\sin\theta_1} b_w \tag{8}$$

when reduction factor is incorporated:

$$N_{C,X} = \zeta\left[Q_f \frac{f_k t_0}{\sin\theta_1} b_w\right] \tag{9}$$

In Eqs. (6)-(9), Q_f is the chord stress function which considers the effect of external chord stresses on the joint resistance and taken as unity in this study. The term f_k is the chord side wall buckling strength and calculated using the buckling curve “c” for cold-formed hollow sections as per EC3

[35].

5. Comparison with design strengths

5.1. General

Tables 11-13 present the comparisons of joint failure resistances ($N_{f,\theta 1}$) of tubular non-90˚ X-joints with the nominal resistances calculated from the EC3 [3] and CIDECT [1]. In addition, in order to directly determine the impact of included angle (θ_1) on the joint resistances, the joint failure resistances ($N_{f,\theta 1}$) of tubular non-90˚ X-joints were also compared with the joint failure resistances (N_f) of tubular 90˚ X-joints of same nominal dimensions and steel grades obtained from Pandey and Young [13]. The $N_{f,\theta 1}/N_{E,X}$ and $N_{f,\theta 1}/N_{C,X}$ ratios checked the applicability of the latest design rules. However, the $N_{f,\theta 1}/N^*_{E,X}$ and $N_{f,\theta 1}/N^*_{C,X}$ ratios checked the applicability of the original design rules developed for NSS tubular X-joints. Therefore, $N_{f,\theta 1}/N_{E,X}$ and $N_{f,\theta 1}/N_{C,X}$ comparisons checked the applicability of the latest design rules for CFHSS tubular non-90˚ X-joint made up of S900 and S960 steel grades. Whereas, $N_{f,\theta 1}/N^*_{E,X}$ and $N_{f,\theta 1}/N^*_{C,X}$ comparisons facilitated in obtaining the reduction factor for CFHSS tubular non-90˚ X-joint made up of S900 and S960 steel grades with respect to the original design rules developed for NSS grades. On the other hand, the ratio $N_{f,\theta 1}/N_f$ compared the joint failure resistances of tubular non-90˚ X-joints with tubular 90˚ X-joints of same nominal dimensions and steel grades. The design rules were considered conservative when the values of these ratios were greater than unity, otherwise, the design rules were considered unconservative.

5.2. RHS-RHS non-90˚ X-joints

The comparisons of joint failure resistances ($N_{f,\theta 1}$) of RHS-RHS non-90˚ X-joints with the nominal resistances of tubular non-90˚ X-joints obtained from the CIDECT [1] and EC3 [3] as well as with the test resistances (N_f) of identical tubular 90˚ X-joints are presented in Tables 11 and 12. It can be noticed that for unequal-width ($\beta \neq 1$) tubular non-90˚ X-joints, the comparison yielded a mixed and unclear trend, when the joint failure resistances ($N_{f,\theta 1}$) of unequal-width ($\beta \neq 1$) test specimens were compared with the nominal resistances obtained from the CIDECT [1] and EC3 [3], without including the reduction factor. The mixed and unclear trend of conservative and unconservative comparison results highlighted the early dependencies on other governing geometric parameters (i.e. 2γ, h_0/t_0 and τ). On the other hand, when the joint failure resistances ($N_{f,\theta 1}$) of RHS-RHS non-90˚ X-joints were compared with the nominal resistances obtained from the CIDECT [1] and EC3 [3], with reduction factor included the values of the ratios $N_{f,\theta 1}/N_{C,X}$

and $N_{f,\theta 1}/N_{E,X}$ are greater than $N_{f,\theta 1}/N^{*}_{C,X}$ and $N_{f,\theta 1}/N^{*}_{E,X}$ ratios because of the reduced nominal resistances. The design rules of the CIDECT [1] and EC3 [3], with reduction factor included, are mostly conservative for unequal-width ($\beta \neq 1$) tubular non-90˚ X-joints, except for X-120×120×3-140×140×4-30˚ and X-120×120×3-150×150×6-50˚. However, for equal-width (β=1) tubular non-90˚ X-joints, the comparison yielded very conservative results when the joint failure resistances ($N_{f,\theta 1}$) of equal-width (β=1) test specimens were compared with the nominal resistances of the CIDECT [1] and EC3 [3], with and without including the reduction factor. Further, it can clearly be seen that the trend of over-conservatism decreased with the increase of the included angle (θ_1). In addition, the joint failure resistances ($N_{f,\theta 1}$) of RHS-RHS non-90˚ X-joints were also compared with the test resistances (N_f) of RHS-RHS 90˚ X-joints of identical nominal dimensions and steel grades. It can be calculated from Table 11 that for θ_1=30˚, the resistances of RHS-RHS non-90˚ X-joints were enhanced by an average of 2.28 times to that of identical RHS-RHS 90˚ X-joints. For θ_1=50˚, the resistances of RHS-RHS non-90˚ X-joints were enhanced by an average of 1.41 times to that of identical RHS-RHS 90˚ X-joints. For θ_1=70˚, the resistances of RHS-RHS non-90˚ X-joints were enhanced by an average of 1.16 times to that of identical RHS-RHS 90˚ X-joints.

Referring to Table 12, for chord face failure mode (F) of RHS-RHS non-90˚ X-joints, the mean values (P_m) of ratios $N_{f,\theta 1}/N^{*}_{E,X}$, $N_{f,\theta 1}/N_{E,X}$, $N_{f,\theta 1}/N^{*}_{C,X}$, $N_{f,\theta 1}/N_{C,X}$ and $N_{f,\theta 1}/N_f$ are 0.92, 1.15, 1.06, 1.18 and 1.93, respectively. The corresponding COVs are 0.094, 0.094, 0.094, 0.094 and 0.418, respectively. Using a resistance factor (ϕ) of 1, the corresponding values of reliability index (β_0) are 1.15, 1.81, 1.69, 2.00 and N.A., respectively. For combined failure mode (F+S) of RHS-RHS non-90˚ X-joints, the mean values (P_m) of ratios $N_{f,\theta 1}/N^{*}_{E,X}$, $N_{f,\theta 1}/N_{E,X}$, $N_{f,\theta 1}/N^{*}_{C,X}$, $N_{f,\theta 1}/N_{C,X}$ and $N_{f,\theta 1}/N_f$ are 0.91, 1.14, 1.00, 1.11 and 1.60, respectively. The corresponding COVs are 0.166, 0.166, 0.144, 0.144 and 0.331, respectively. Using a resistance factor (ϕ) of 1, the corresponding values of reliability index (β_0) are 1.17, 1.86, 1.67, 2.02 and N.A., respectively. For chord side wall failure mode (S) of RHS-RHS non-90˚ X-joints, the mean values (P_m) of ratios $N_{f,\theta 1}/N^{*}_{E,X}$, $N_{f,\theta 1}/N_{E,X}$, $N_{f,\theta 1}/N^{*}_{C,X}$, $N_{f,\theta 1}/N_{C,X}$ and $N_{f,\theta 1}/N_f$ are 6.06, 7.57, 4.88, 5.42 and 1.49, respectively. The corresponding COVs are 0.322, 0.322, 0.321, 0.321 and 0.293, respectively. Using a resistance factor (ϕ) of 1, the corresponding values of reliability index (β_0) are 4.41, 4.85, 4.08, 4.28 and N.A., respectively.

5.3. CHS-RHS non-90˚ X-joints

Table 13 presents the comparisons of the joint failure resistances ($N_{f,\theta 1}$) of CHS-RHS non-90˚ X-joints with the nominal resistances obtained from the CIDECT [1] and EC3 [3] as well

as with the test resistances (N_f) of identical CHS-RHS 90˚ X-joints. From Table 13, it can be seen that when the joint failure resistances ($N_{f,\theta 1}$) of CHS-RHS non-90˚ X-joints are compared with the nominal resistances obtained from the EC3 [3] without using any reduction factor, the design rules are unconservative for tubular non-90˚ X-joints with included angle θ_1=30˚ and 50˚ and conservative for θ_1=70˚. When the joint failure resistances ($N_{f,\theta 1}$) of CHS-RHS non-90˚ X-joints are compared with the nominal resistances obtained from the EC3 [3] by including the reduction factor, the design rules are conservative for all the included angles covered in this investigation, i.e., θ_1=30˚, 50˚ and 70˚. Similarly, on comparing the joint failure resistances ($N_{f,\theta 1}$) of CHS-RHS non-90˚ X-joints with the nominal resistances obtained from the CIDECT [1] without using any reduction factor, the design rules are unconservative for tubular non-90˚ X-joints with included angle θ_1=30˚, and conservative when θ_1 increased to 50˚ and 70˚. Also, when the joint failure resistances ($N_{f,\theta 1}$) of CHS-RHS non-90˚ X-joints are compared with the nominal resistances of the CIDECT [1] obtained by including the reduction factor, the design rules are in general conservative. At large values of the included angle (θ_1), the increase in test resistance was significantly more than the corresponding increase in the nominal resistance. Therefore, due to this reason, the design rules become increasingly conservative with the increase of included angle (θ_1) for CHS-RHS test specimens.

Furthermore, the joint failure resistances ($N_{f,\theta 1}$) of CHS-RHS non-90˚ X-joints were also compared with the test resistances (N_f) of CHS-RHS 90˚ X-joints of identical nominal dimensions and steel grades. It can be calculated from Table 13 that for θ_1=30˚, the resistances of CHS-RHS non-90˚ X-joints were enhanced by an average of 2.15 times to that of identical CHS-RHS 90˚ X-joints. For θ_1=50˚, the resistances of CHS-RHS non-90˚ X-joints were enhanced by an average of 1.29 times to that of identical CHS-RHS 90˚ X-joints. For θ_1=70˚, the resistances of CHS-RHS non-90˚ X-joints were enhanced by an average of 1.11 times to that of identical CHS-RHS 90˚ X-joints. Referring to Table 13, for CHS-RHS non-90˚ X-joints, the mean values (P_m) of ratios $N_{f,\theta 1}/N^*_{E,X}$, $N_{f,\theta 1}/N_{E,X}$, $N_{f,\theta 1}/N^*_{C,X}$, $N_{f,\theta 1}/N_{C,X}$ and $N_{f,\theta 1}/N_f$ are 0.99, 1.24, 1.07, 1.19 and 1.44, respectively. The corresponding COVs are 0.146, 0.146, 0.142, 0.142 and 0.314, respectively. Using a resistance factor (ϕ) of 1, the corresponding values of reliability index (β_0) are 1.50, 2.21, 1.88, 2.22 and N.A., respectively.

5.4. Discussion of comparison results

For tubular non-90˚ X-joints with small to medium β ratio (β < 0.6), the deformation limit criterion controlled the joint resistance, as the load vs deformation curves for such test specimens were monotonically increasing without any clear ultimate load. The existing design rule for the

chord face failure mode (F) of X-joint is based on a lower bound simplified yield line model. The yield line model was developed by ignoring the effects of membrane action, strain hardening of the material and weld leg size, i.e., the model assumed small deformations just sufficient to cause the material yielding. Nonetheless, the model showed a convincing validation for X-joints with steel grades up to S355 [36]. The stress-strain behaviour of S900 and S960 steel grades tubular members significantly deviates from that of NSS grades. This change in the material behaviour could change the response of CFHSS tubular non-90˚ X-joints, particularly in the deformation and propagation of chord face yield line patterns and development of chord face membrane actions, compared to the mild steel counterparts. For small to medium β ratio (β < 0.6), NSS X-joints are expected to undergo relatively larger chord connecting face deformation compared to their corresponding HSS X-joints. For CFHSS tubular non-90˚ X-joints with small to medium β ratio, and particularly for large 2γ ratio (2γ > 20), the current deformation limit ($0.03b_0$) seems not sufficient to develop plastic hinges in the chord connecting face. Therefore, the strength of HSS material from the inelastic region to yield strength could not be effectively utilised due to the existing $0.03b_0$ deformation limit criterion, and thus, the current simplified yield line model, which takes into account of only material yield strength, becomes unconservative.

However, for equal-width (β=1) CFHSS tubular non-90˚ X-joints, CIDECT [1] and EC3 [3] design rules are clearly over-conservative. The existing design rule for the chord side wall failure mode (S) of X-joint is based on a simplified combined web bearing and buckling analytical model. The findings of Pandey and Young [11-13] proved that the existing chord side wall failure joint resistance expression becomes increasingly conservative with the increase of chord side wall slenderness ratio (h_0/t_0) for tubular joints made up of S900 and S960 steel grades. The reason for this observation is due to the assumption of chord side wall a pin-ended column of effective length (h_0-$2t_0$). In this study, the trend of over-conservativism decreased with the increase of included angle (θ_1), as the decrease in test resistance is significantly more than the corresponding decrease in the nominal resistance for equal-width (β=1) RHS-RHS non-90˚ X-joints. For all the three values of included angle (θ_1), the equal-width (β=1) tubular non-90˚ X-joints have shown a clear peak load at an early deformation stage in their corresponding load vs deformation curves, and thus, governed the joints resistances. The authors are of the opinion that the behaviour of test specimens failed by chord side wall failure mode (S) is a complex phenomenon and may involve column buckling or plate buckling behaviour depending on the chord side wall slenderness ratio (h_0/t_0). By definition, tubular X-joints are the joints where the normal component of brace member force is transmitted through the chord member and is equilibrated by the brace member(s) on the opposite side [1]. However, for tubular non-90˚ X-joints, a significant portion ($N_1\text{Cos}\theta_1$) of the applied brace axial force (N_1) was transmitted to other brace member by the shearing of the chord member. The chord

shearing action became more effective with the decrease of the included angle (θ_1) between brace and chord members of tubular non-90˚ X-joints. Unlike tubular 90˚ X-joints, where the total brace axial compression load (N_1) contributed towards the buckling of both chord side walls, only the $N_1\text{Sin}\theta_1$ component of the total brace axial load (N_1) contributed towards the normal buckling of both chord side walls for tubular non-90˚ X-joints, and thus, responsible for the delayed chord side wall buckling and increased static joint resistance.

6. Conclusions

A test programme on cold-formed high strength steel tubular non-90˚ X-joints subjected to brace axial compression is presented in this paper to investigate the static resistances and load vs deformation behaviour of these joints. A total of three sets of tubular non-90˚ X-joints were designed, wherein the included angle (θ_1) between brace and chord members were kept as 30˚, 50˚ and 70˚. Two configurations of tubular non-90˚ X-joints were fabricated, namely RHS-RHS and CHS-RHS. The welding of brace and chord members was performed using the automatic gas metal arc welding process. A total of 26 tubular non-90˚ X-joints, including 18 RHS-RHS and 8 CHS-RHS test specimens, were investigated in this experimental programme. The joint failure resistances ($N_{f,\theta 1}$) of tubular non-90˚ X-joints were compared with the nominal resistances obtained from the CIDECT [1] and EC3 [3], with and without including the respective recommended reduction factors. Furthermore, material properties from the transverse compression coupons and from the weld heat affected regions were also investigated. Following are the key conclusions:

- The ultimate strengths of tensile coupons extracted from the weld heat affected regions of S960 steel grade TMCP tubular members of thicknesses 3, 4 and 6 mm were reduced as much as by 32%, 25% and 14% in the first 6 mm regions from the weld toe, respectively.
- For all tubular non-90˚ X-joints, maximum chord face indentation was observed at the toe location, while the chord face indentation at the heel location was trivial.
- On increasing the value of included angle (θ_1), initial stiffness, joint resistance and post-yield stiffness of tubular non-90˚ X-joints reduced. The reductions were sharper during the initial increase of the included angle (θ_1).
- The joint failure resistances of tubular non-90˚ X-joints were dropped by an average of 38.5% and 48.9% when the included angle (θ_1) increased from 30° to 50° and 30° to 70°, respectively.
- For RHS-RHS non-90˚ X-joints, the average joint resistances were enhanced by 2.28, 1.41 and 1.16 times of identical RHS-RHS 90˚ X-joints for the included angle (θ_1) of 30°, 50° and 70°, respectively. Whereas, for CHS-RHS non-90˚ X-joints, the average joint resistances were

enhanced by 2.15, 1.29 and 1.11 times of identical CHS-RHS 90˚ X-joints for the included angle (θ_1) of 30°, 50° and 70°, respectively.

- Three types of failure modes were observed in this investigation, namely chord face failure (F), chord side wall failure (S) and a combination of these two failures (F+S) modes.
- The comparisons showed that the existing design rules of tubular X-joints given in the CIDECT [1] and EC3 [3] are not capable of providing accurate and reliable predictions for cold-formed high strength steel tubular non-90˚ X-joints made up of S900 and S960 steel grades.
- For tubular non-90˚ X-joints with $\beta \neq 1$, a clear conservative or unconservative trend could not be established with the available test results. However, for equal-width ($\beta=1$) tubular non-90˚ X-joints, the design rules given in the CIDECT [1] and EC3 [3] were very conservative. The trend of over-conservativism decreased with the increase of included angle (θ_1) and increased with the increase of chord side wall slenderness ratio (h_0/t_0).

Acknowledgements

The authors are grateful to SSAB Europe Oy for providing the cold-formed high strength steel tubes. Thanks are due to Wo Lee Steel Co. Ltd. (HK) for their help in the automatic welding of the test specimens. The research work described in this paper was supported by a grant from the Research Grants Council of the Hong Kong Special Administrative Region, China (Project No. 17210218).

References

[1] Packer JA, Wardenier J, Zhao XL, van der. Vegte GJ and Kurobane Y. Design guide for rectangular hollow section (RHS) joints under predominantly static loading, Comite´ International pour le Developpement et l'Etude de la Construction TuECbulaire (CIDECT), Design Guide No. 3, 2nd edn., LSS Verlag, Dortmund, Germany, 2009.
[2] IIW Doc. XV-1402-12 and IIW Doc. XV-E-12-433, Static design procedure for welded hollow section joints – Recommendations, International Institute of Welding, Paris, France, 2012.
[3] EN 1993-1-8, Eurocode 3: Design of steel structures–Part 1-8: Design of joints, European Committee for Standardization (CEN), Brussels, Belgium, 2005.
[4] Specification for Structural Steel Buildings. ANSI/AISC 360-16, American Institute of Steel Construction, Chicago, Illinois, USA, 2016.
[5] Cold-formed Stainless Steel structures. AS/NZS 4673:2001, Australian/New Zealand Standard, Sydney, Australia, 2001.
[6] Packer JA and Henderson JE. Hollow Structural Section Connections and Trusses – A Design Guide, Canadian Institute of Steel Construction, Willowdale, Ontario, Canada, 1997.
[7] Welding–static design procedure for hollow section joints-Recommendations. BS ISO 14346, British Standard International Standard, Geneva, Switzerland, 2013.
[8] Packer JA, Wardenier J, Kurobane Y, Dutta D and Yeomans N. Design guide for rectangular hollow section (RHS) joints under predominantly static loading, CIDECT Design Guide No. 3, 1st Edition, Comite´ International pour le Developpement et l'Etude de la Construction Tubulaire, Verlag TUV Rheinland, Cologne, Germany, 1992.
[9] Design recommendations for hollow section joints. IIW Doc. XV-491-81, International Institute of Welding, 1st Edition, Oporto, Portugal, 1981.
[10] Wardenier J, Packer JA, Zhao XL and van der Vegte GJ. Background of the new RHS joint strength equations in the IIW (2009) recommendations. Proceedings of the 13th International Symposium on Tubular Structures, Hong Kong, 403-412, 2010.
[11] Pandey M and Young B. Tests of cold-formed high strength steel tubular T-joints. Thin-Walled Struct 2019;143:106200.
[12] Pandey M and Young B. Compression capacities of cold-formed high strength steel tubular T-joints. J Constr Steel Res 2019;162:105650.
[13] Pandey M and Young B. Structural performance of cold-formed high strength steel tubular X-Joints under brace axial compression. Engineering Structures, 2020; 208:109768.
[14] Lan X, Chan TM, Young B. Experimental study on the behaviour and strength of high strength steel CHS T-and X-joints. Engineering Structures, 206, 110182, 2020.
[15] Feldmann M, Schillo N, Schaffrath S, Virdi K, Björk T, Tuominen N, et al. Rules on high strength steel. Luxembourg: Publications Office of the European Union; 2016.
[16] Havula J, Garifullin M, Heinisuo M, Mela K, Pajunen S. Moment-rotation behavior of welded tubular high strength steel T joint. Eng Struct 2018;172:523–37.
[17] SSAB, Strenx Tube 900 MH. Data Sheet 2042, Sweden, 2017.
[18] SSAB, Strenx Tube 960 MH. Data Sheet 2043, Sweden, 2017.
[19] Cold formed welded structural hollow sections of non-alloy and fine grain steels-Part 1: Technical delivery conditions. prEN 10219-1:2016, European Committee for Standardization, CEN, Brussels, Belgium, 2016.
[20] ASTM E8/E8M, Standard Test Methods for Tension Testing of Metallic Materials, American

Society for Testing and Materials (ASTM), West Conshohocken, PA, USA, 2016.
[21] AWS D1.1/D1.1M, Structural Welding Code – Steel, American Welding Society (AWS), Miami, USA, 2015.
[22] AWS A5.28/A5.28M, Specification for Low-Alloy Steel Electrodes and Rods for Gas Shielded Arc Welding, American Welding Society (AWS), Miami, USA, 2015.
[23] Teh LH and Rasmussen KJR. Strength of arc-welded T-joints between equal width cold-formed RHS, J. Constr. Steel Res. 63;571-579, 2007.
[24] CIDECT, Construction with hollow steel sections, Comite´ International pour le Developpement et l'Etude de la Construction Tubulaire, British Steel Plc., Corby, UK, 1984.
[25] Stroetmann R, Kastner T, Halsig A, Mayr P. Mechanical properties and a new design approach for welded joints at high strength steels. Hong Kong:Engineering Research and Practice for Steel Construction; 2018:79–90.
[26] Dilthey U. Schweißtechnische Fertigungsverfahren 2 – Verhalten der Werkstoffe beim Schweißen. Auflage, Berlin, Heidelberg, New York: Springer-Verlag, 2006.
[27] Javidan F, Heidarpour A, Zhao XL, Hutchinson CR, Minkkinen J. Effect of weld on the mechanical properties of high strength and ultra-high strength steel tubes in fabricated hybrid sections. Eng Struct 2016;118:16–27.
[28] Li GQ, Lyu H, Zhang C. Post-fire mechanical properties of high strength Q690 structural steel, J. Constr. Steel Res. 132:108-116, 2017.
[29] Kang L, Suzuki M, Ge H, Wu B. Experiment of ductile fracture performances of HSSS Q690 after a fire. J. Constr. Steel Res. 146;2018: 109-121, 2018.
[30] Wang XQ, Tao Z, Hassan MK. Post-fire behaviour of high-strength quenched and tempered steel under various heating conditions. J. Constr. Steel Res. 164;2020:105785, 2020.
[31] AISI S100, North American Specification for the design of cold-formed steel structural members, American Iron and Steel Institute (AISI), Washington, D.C., USA, 2016.
[32] EN 1990, Eurocode: Basis of structural design, European Committee for Standardization (CEN), Brussels, Belgium, 2002.
[33] ASCE/SEI 7, Minimum Design Loads for Buildings and Other Structures, American Society of Civil Engineers (ASCE), New York, USA, 2016.
[34] EN 1993-1-12, Eurocode 3: Design of Steel Structures – Part 1-12: Additional Rules for the Extension of EN 1993 Up to Steel Grades S700, European Committee for Standardization (CEN), Brussels, Belgium, 2007.
[35] EN 1993-1-1, Eurocode 3: Design of steel structures–Part 1-1: General rules and rules for buildings, European Committee for Standardization (CEN), Brussels, Belgium, 2005.
[36] Wardenier J. Hollow Section Joints, Delft University Press, Delft, 1982.

a. Set-1 (θ_1=30˚)

b. Set-2 (θ_1=50˚)

c. Set-3 (θ_1=70˚)

Fig. 1. Tubular non-90˚ X-joints for set-1, 2 and 3

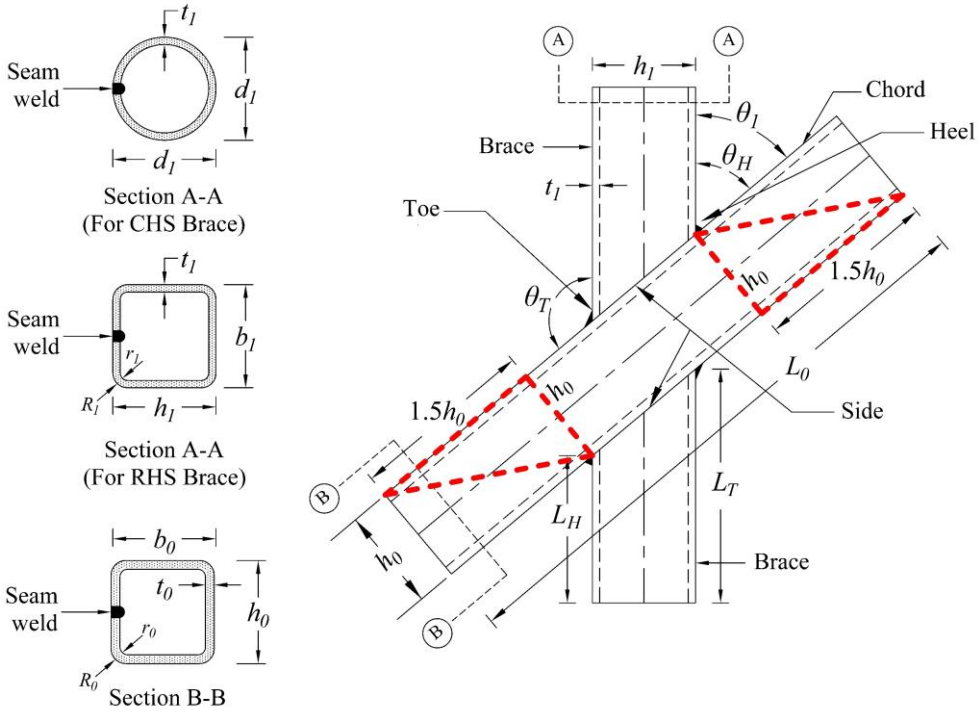

Fig. 2. Definitions of symbols for tubular non-90˚ X-joints

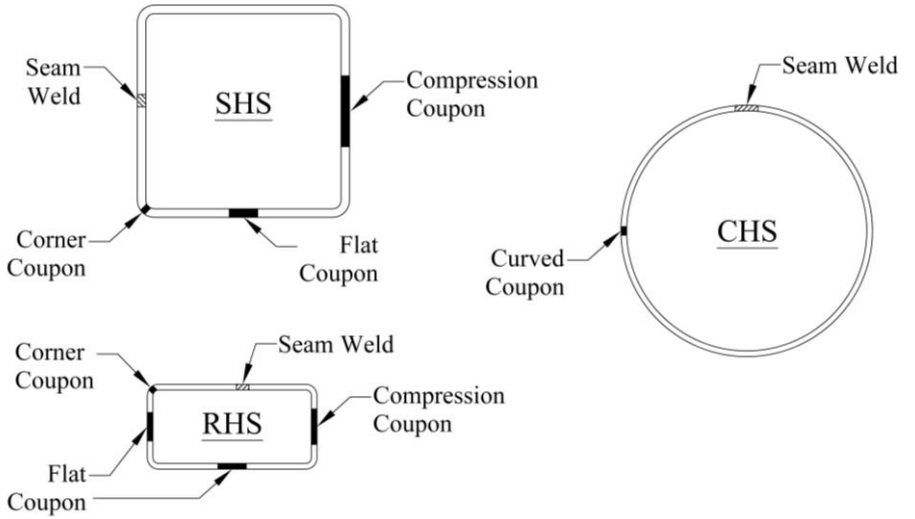

Fig. 3. Locations of coupons extracted from different regions of tubes

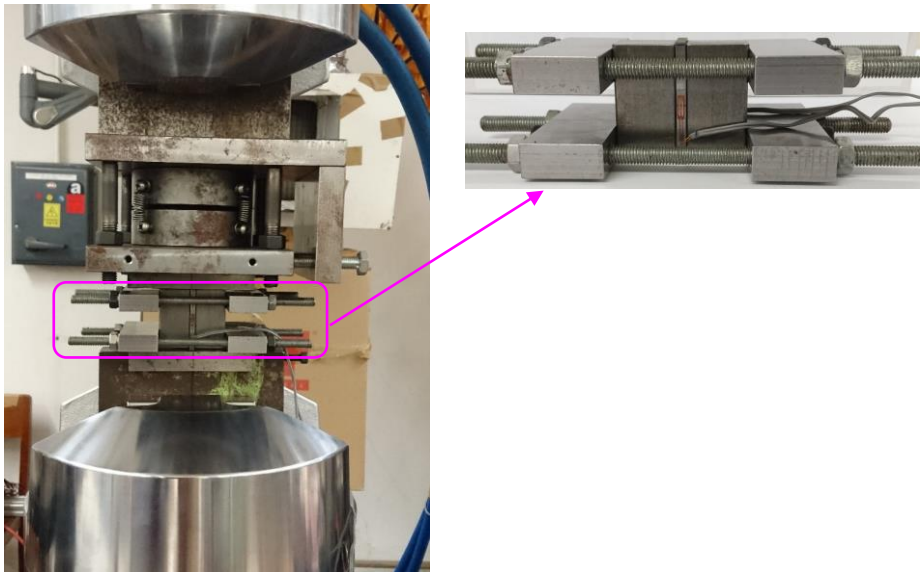

Fig. 4. Test-setup for compression coupon

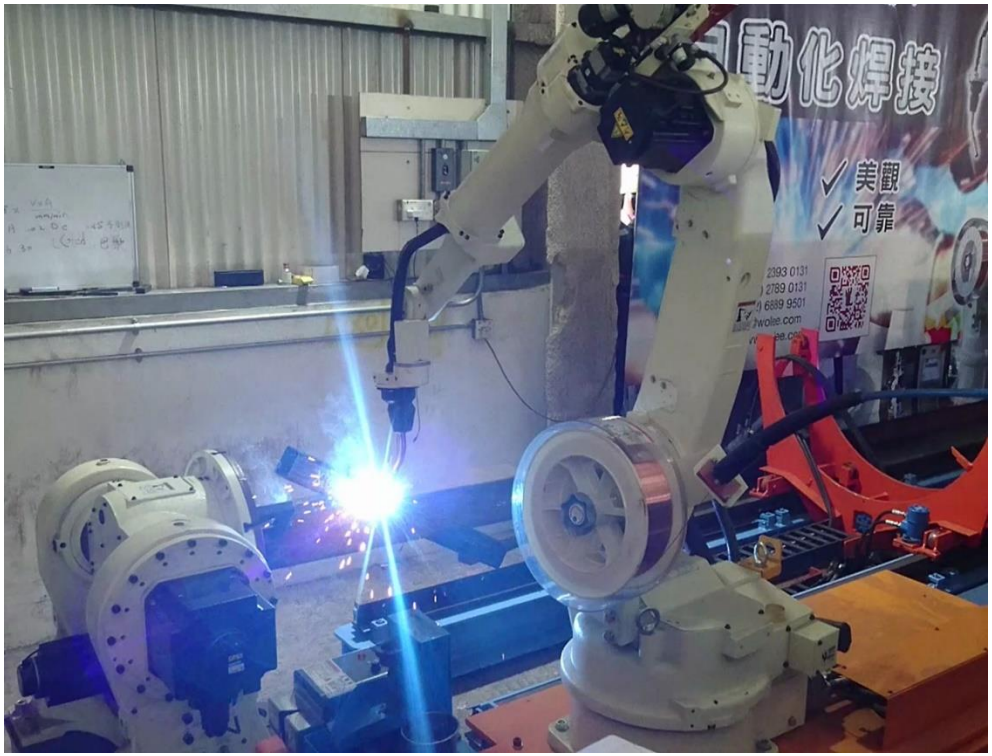

Fig. 5. Automatic GMAW of tubular non-90˚ X-joint

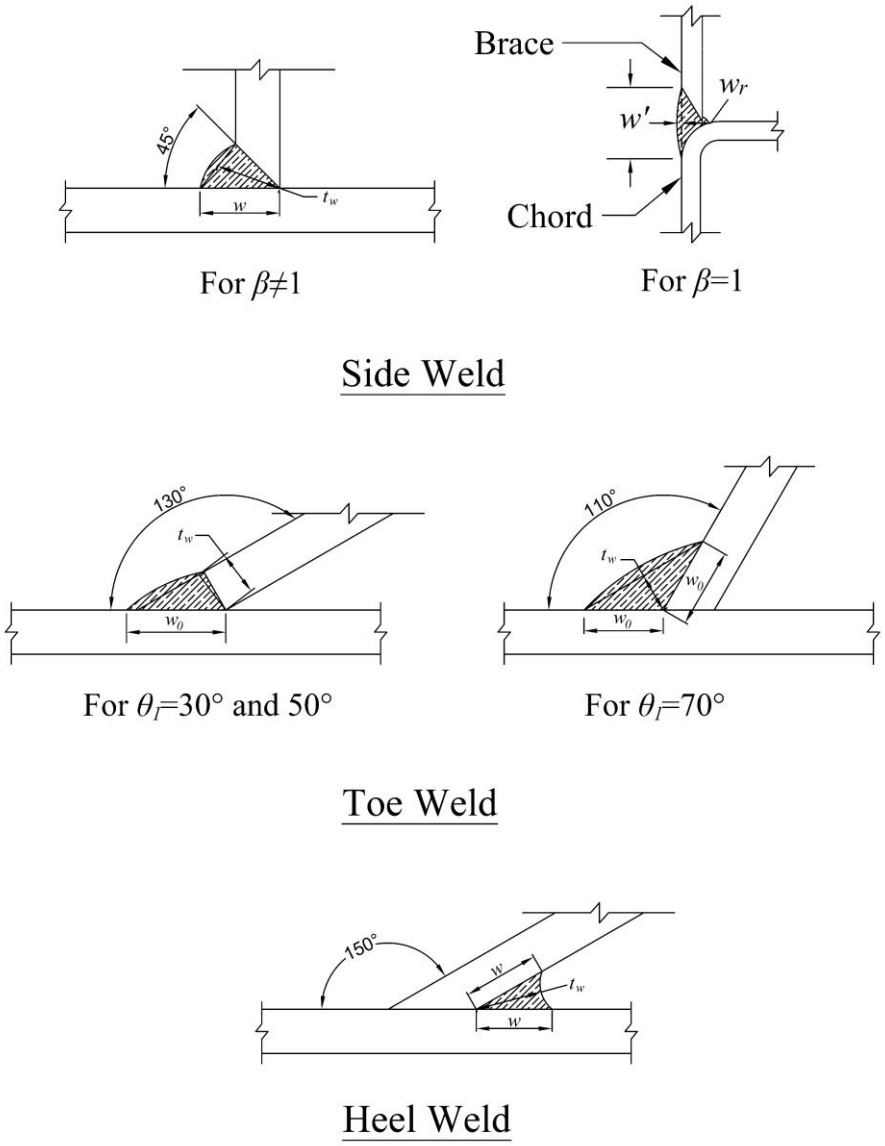

Fig. 6. Typical weld profiles for different regions of tubular non-90˚ X-joints

a. For 3 mm thickness b. For 4 mm thickness c. For 6 mm thickness

Fig. 7. Tubular test specimens of different thicknesses for WHAR investigation

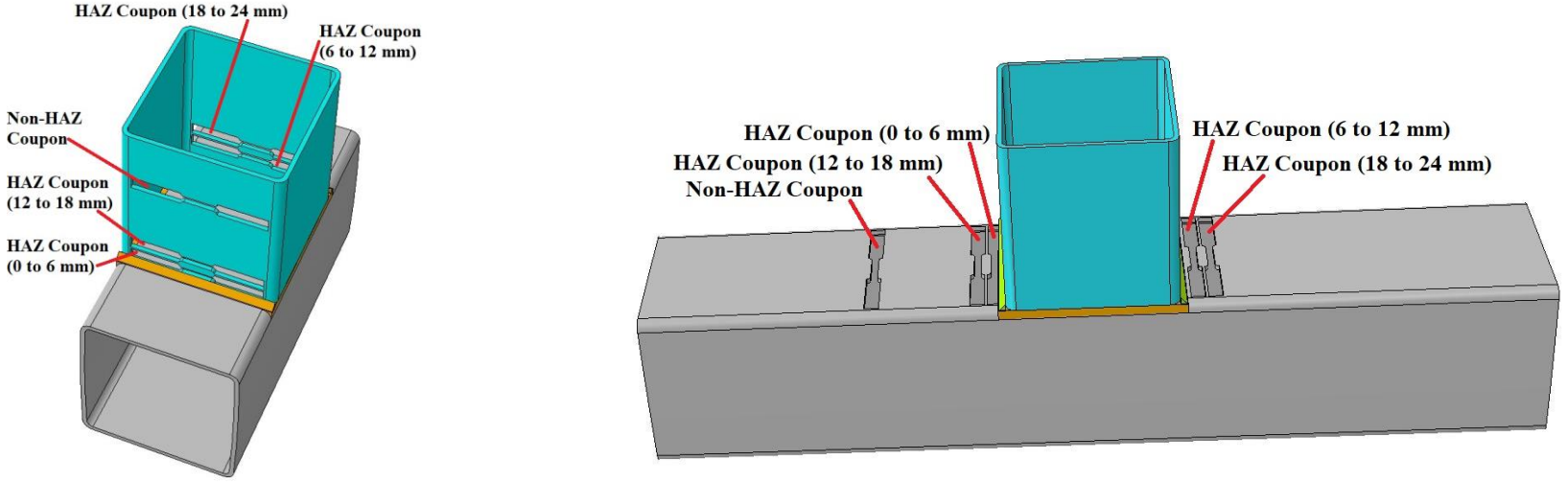

(a) WHAR coupons taken from Brace (for 3 and 4 mm) (b) WHAR coupons taken from Chord (for 6 mm)

Fig. 8. Extracted locations of HAZ and non-HAZ tensile coupons

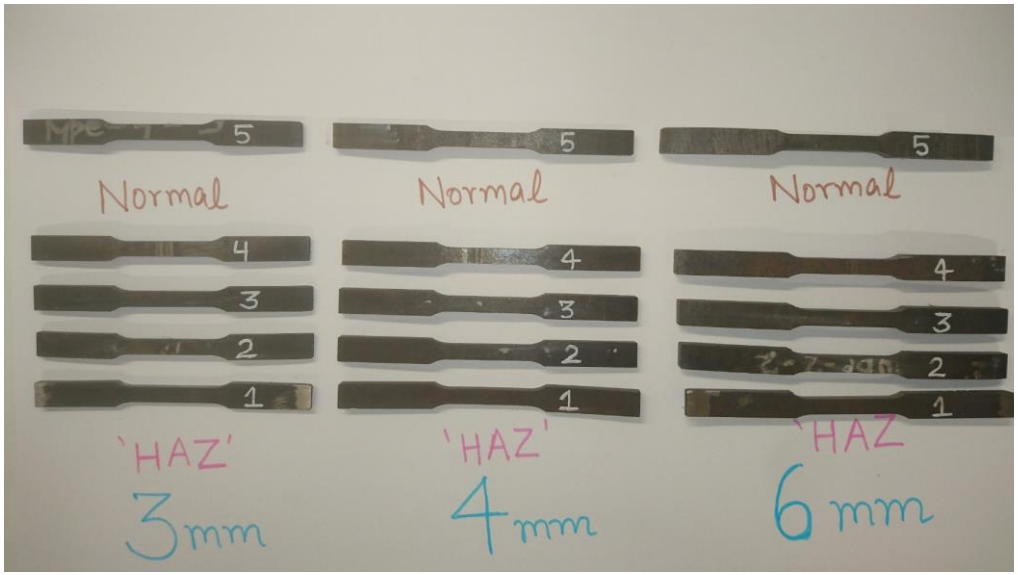

Fig. 9. HAZ and Non-HAZ tensile coupons before tests

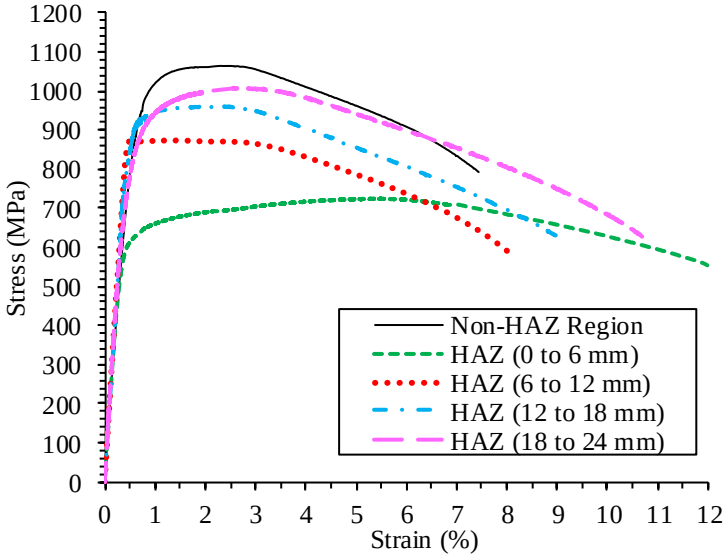

Fig. 10. Static stress-strain curves from WHAR of 3 mm thickness

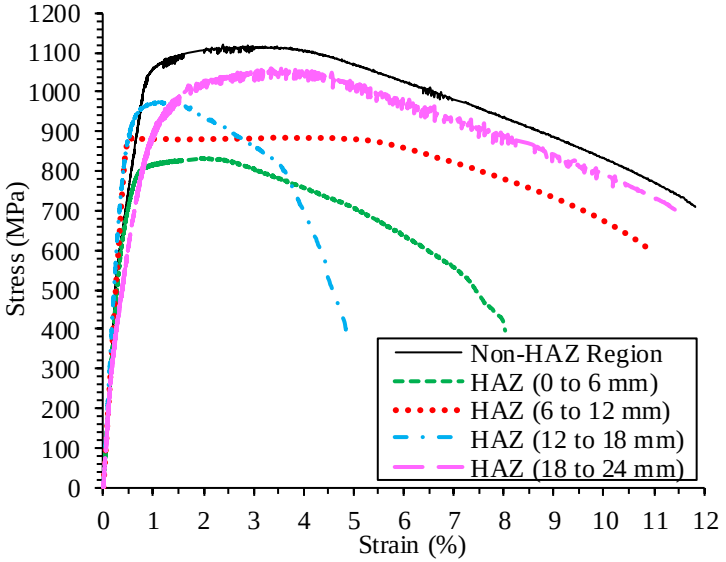

Fig. 11. Static stress-strain curves from WHAR of 4 mm thickness

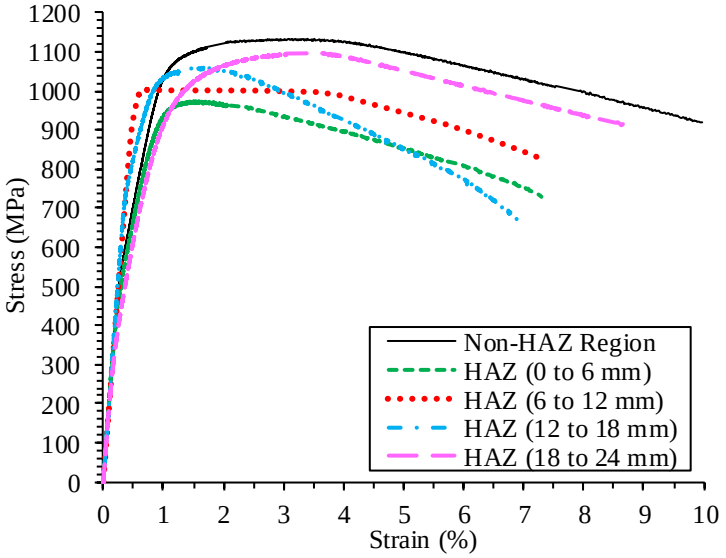

Fig. 12. Static stress-strain curves from WHAR of 6 mm thickness

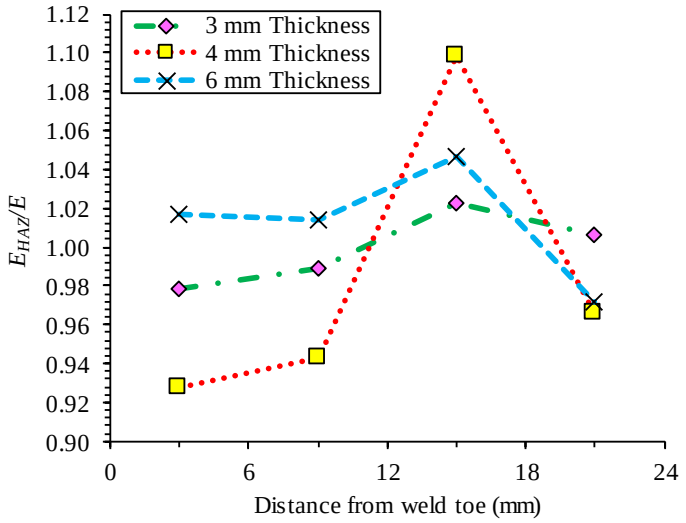

a. Young's Modulus

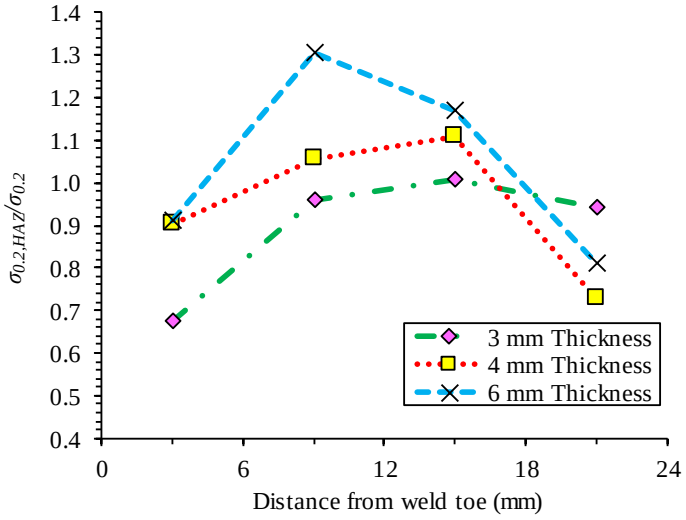

b. Yield strength

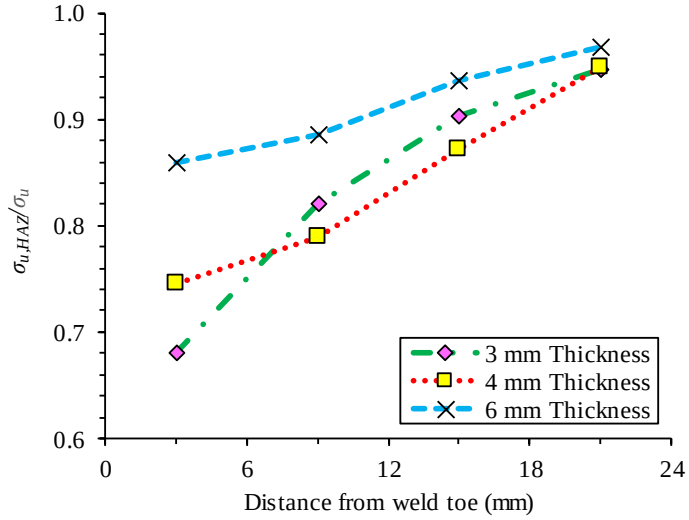

c. Ultimate strength

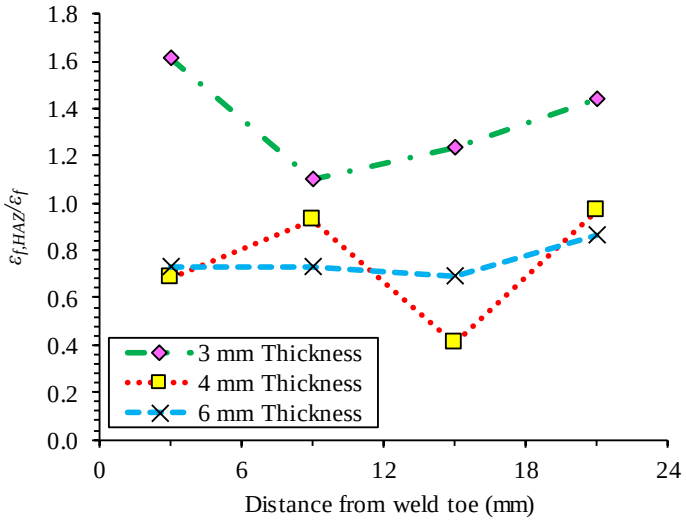

d. Fracture strain

Fig. 13. Variation of WHAR residual factors for different material properties

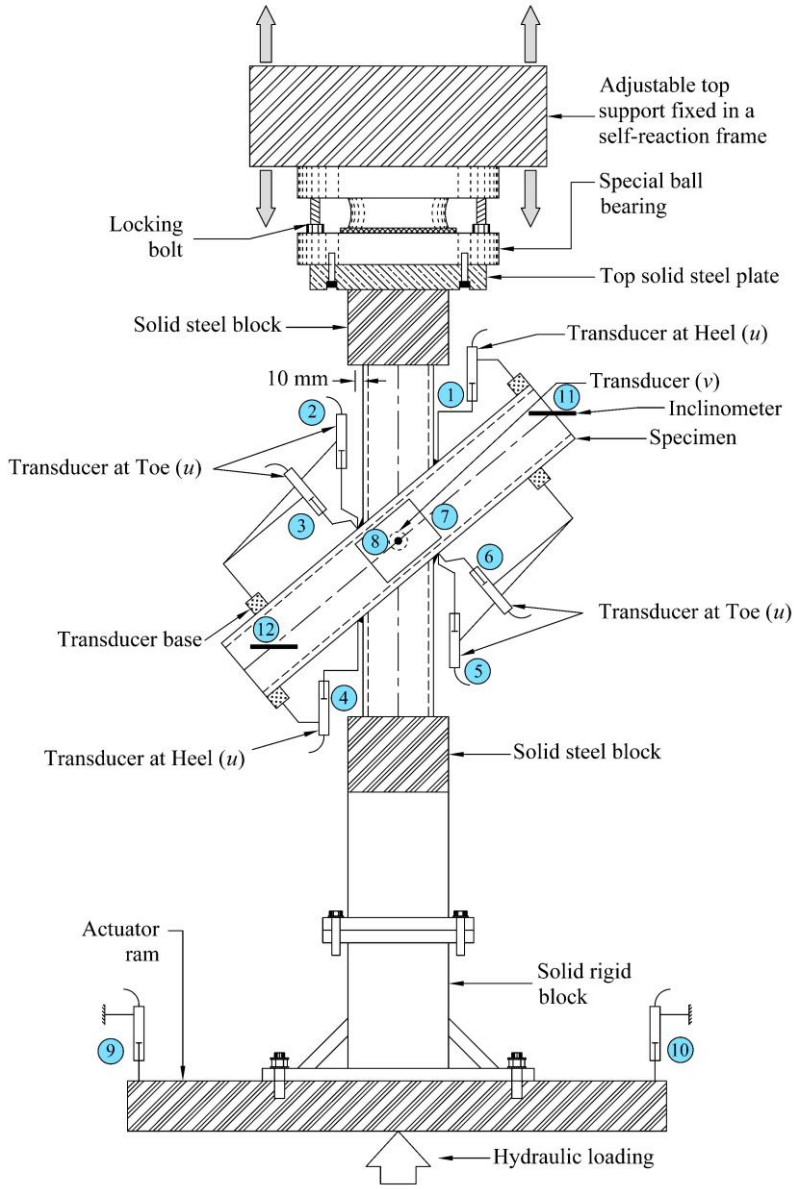

Fig. 14 Schematic sketch of the test rig for tubular non-90˚ X-joint

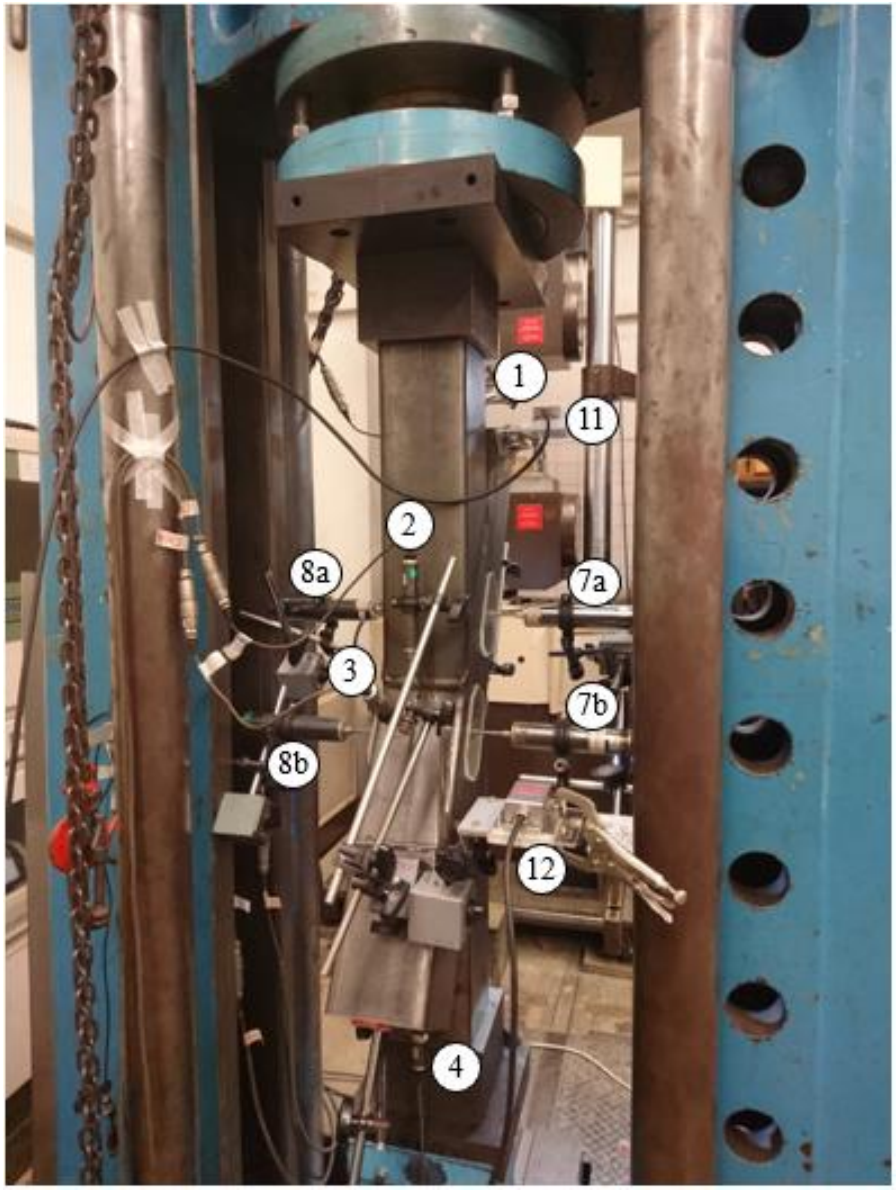

Fig. 15. Photo of tubular non-90˚ X-joint test setup in 1000 kN machine

Fig. 16. Photo of tubular non-90˚ X-joint test setup in 5000 kN machine

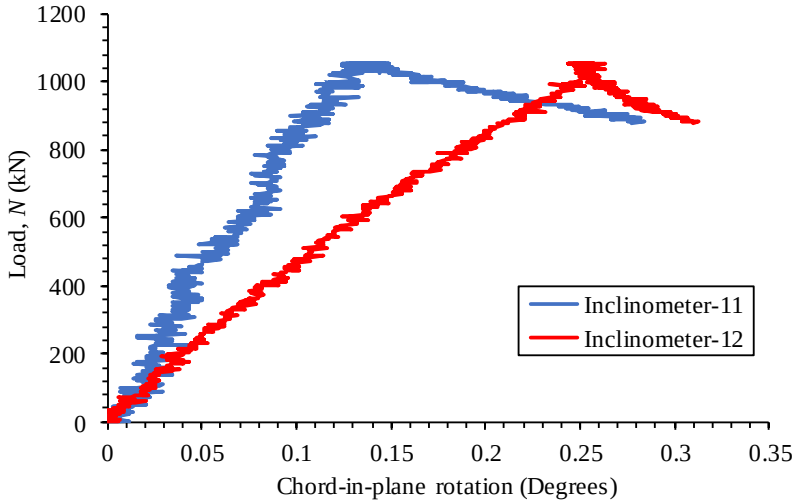

a. For X-120×120×4-120×120×4-30°

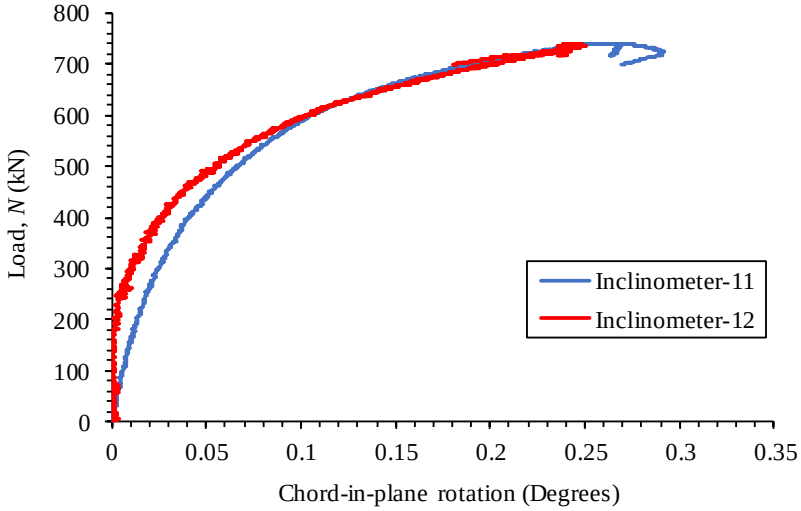

b. For X-120×120×3-150×150×6-50°

Fig. 17. Variations of applied load vs chord-in-plane rotation

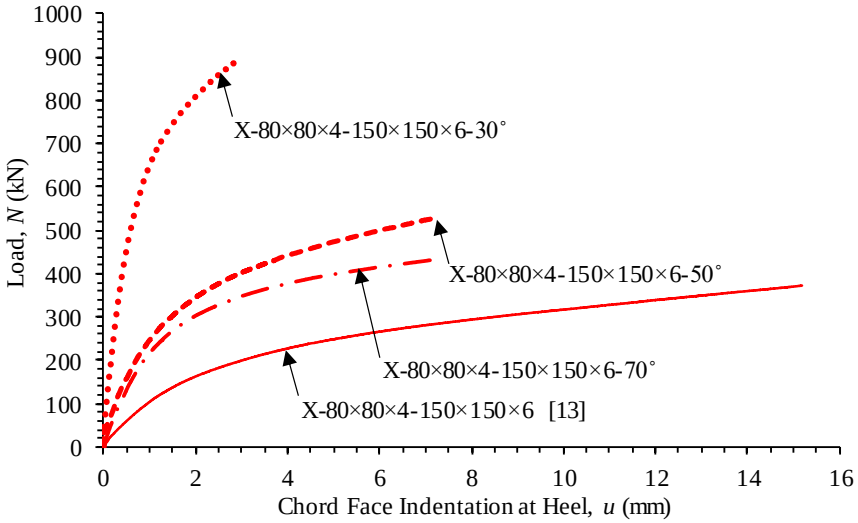

a. Load vs Chord face indentation curves at heel

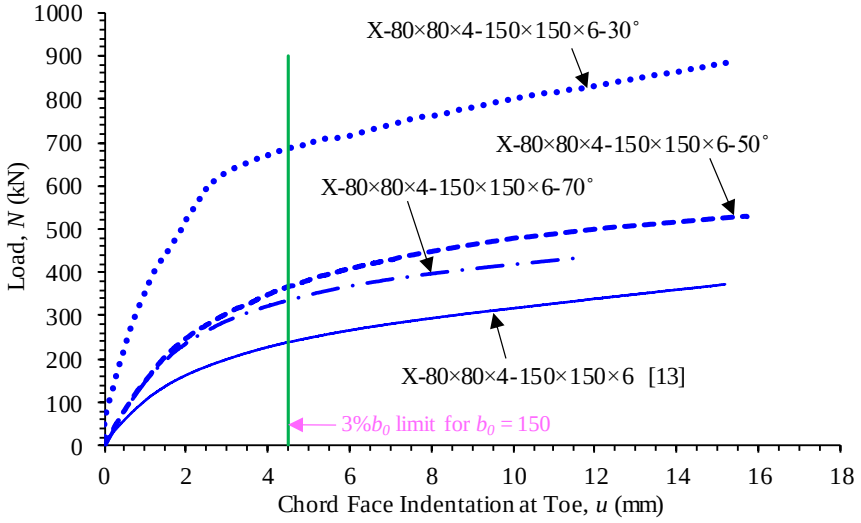

b. Load vs Chord face indentation curves at toe

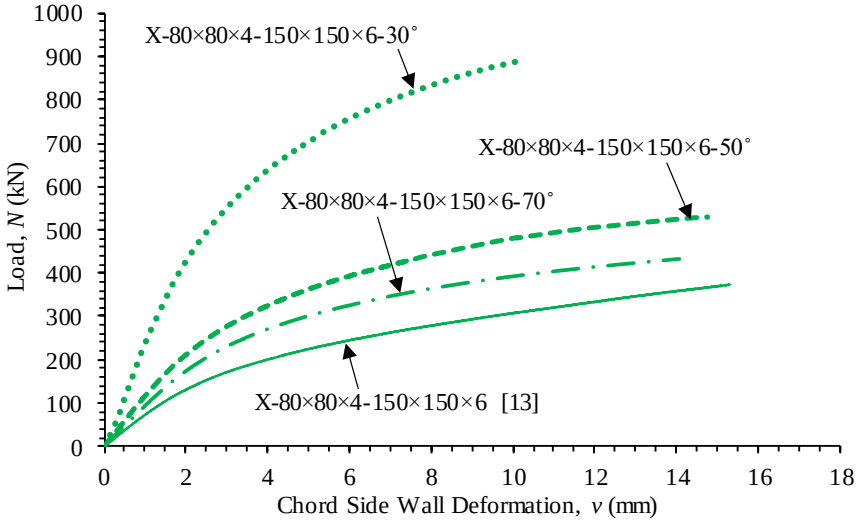

c. Load vs Chord side wall deformation curves

Fig. 18. Load vs deformation curves for RHS-RHS non-90˚ X-joints with chord face failure mode (F)

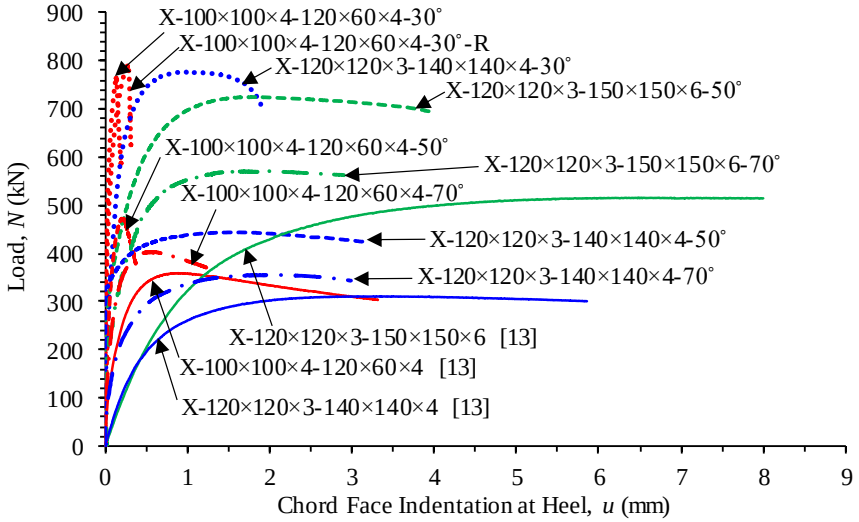

a. Load vs Chord face indentation curves at heel

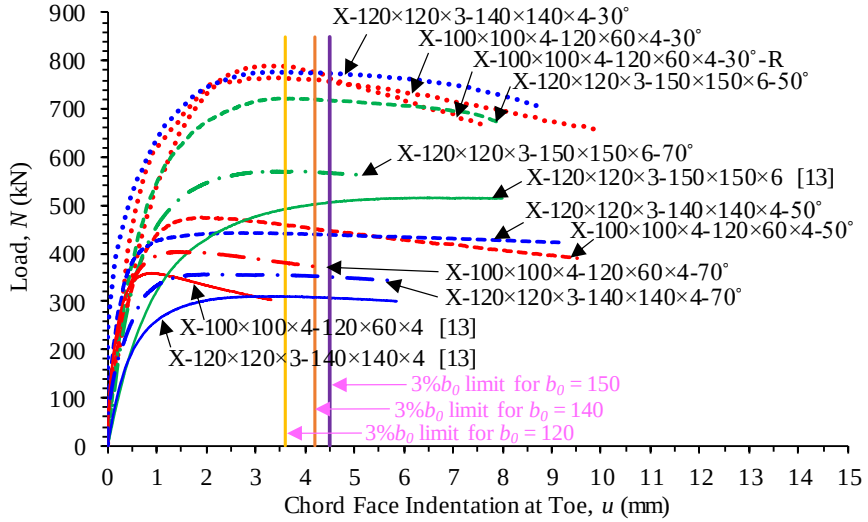

b. Load vs Chord face indentation curves at toe

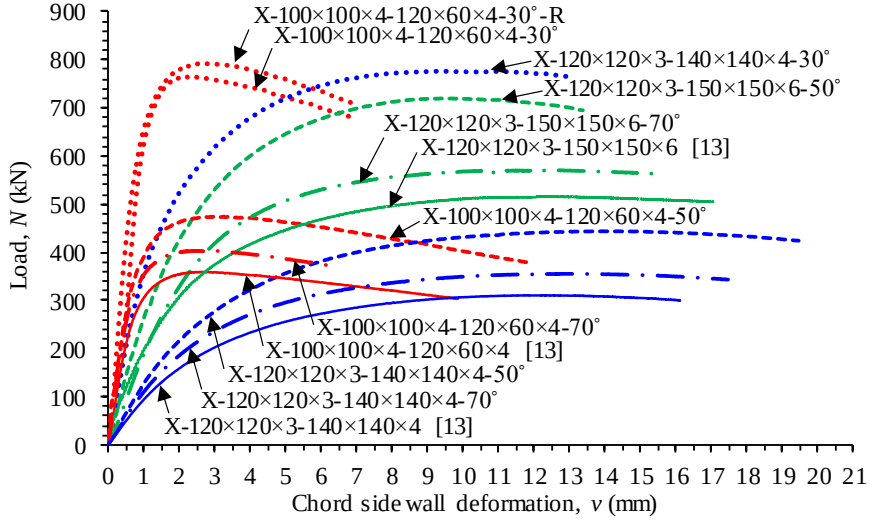

c. Load vs Chord side wall deformation curves

Fig. 19. Load vs deformation curves for RHS-RHS non-90˚ X-joints with combined failure mode (F+S)

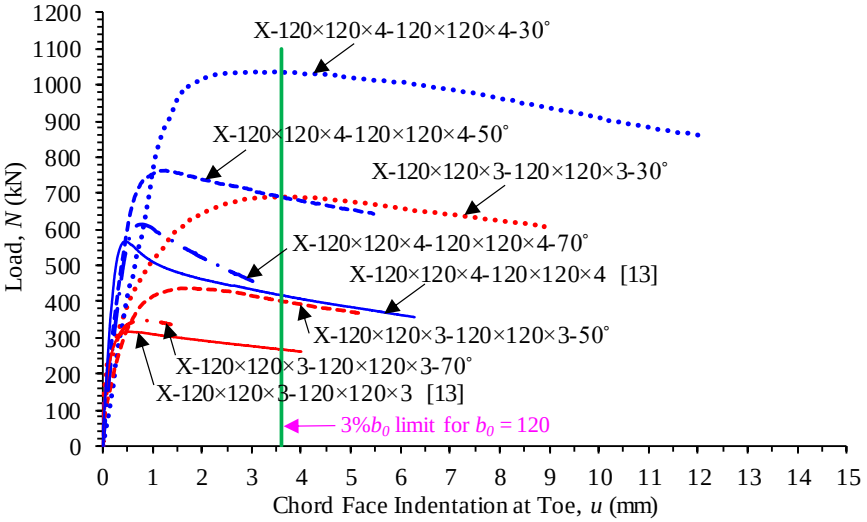

a. Load vs Chord face indentation curves at toe

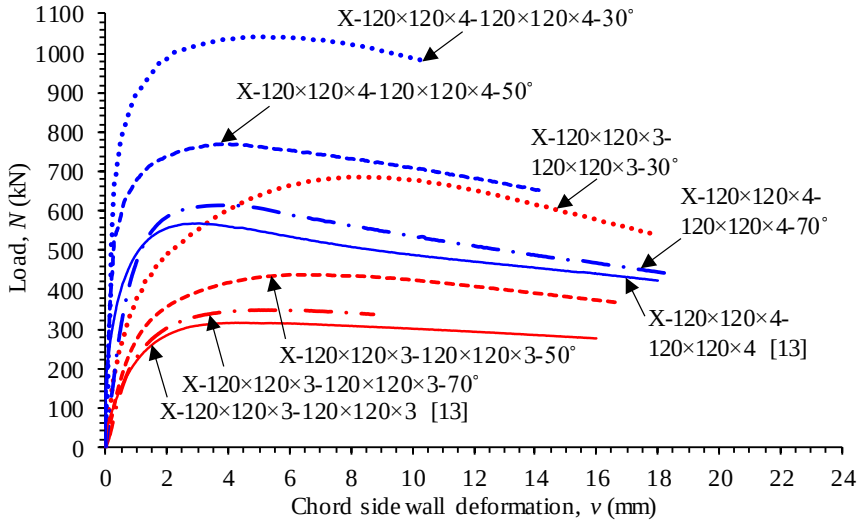

b. Load vs Chord side wall deformation curves

Fig. 20. Load vs deformation curves for RHS-RHS non-90˚ X-joints with chord side wall failure mode (S)

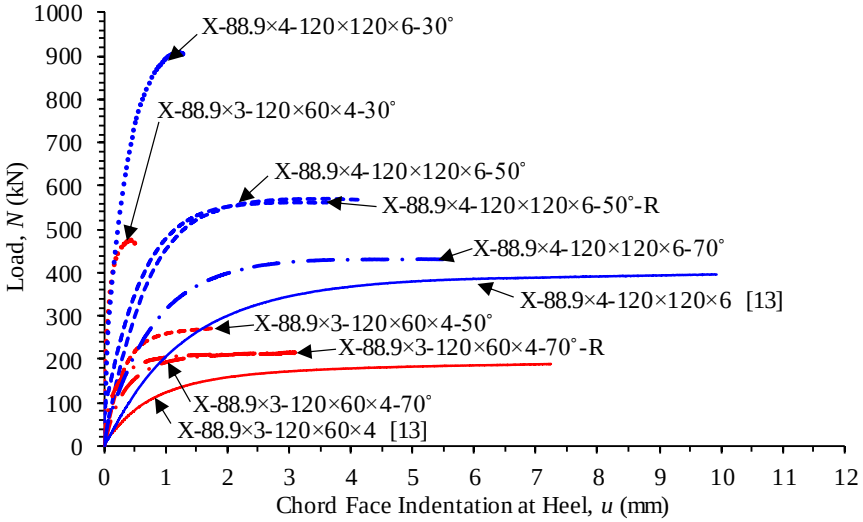

a. Load vs Chord face indentation curves at heel

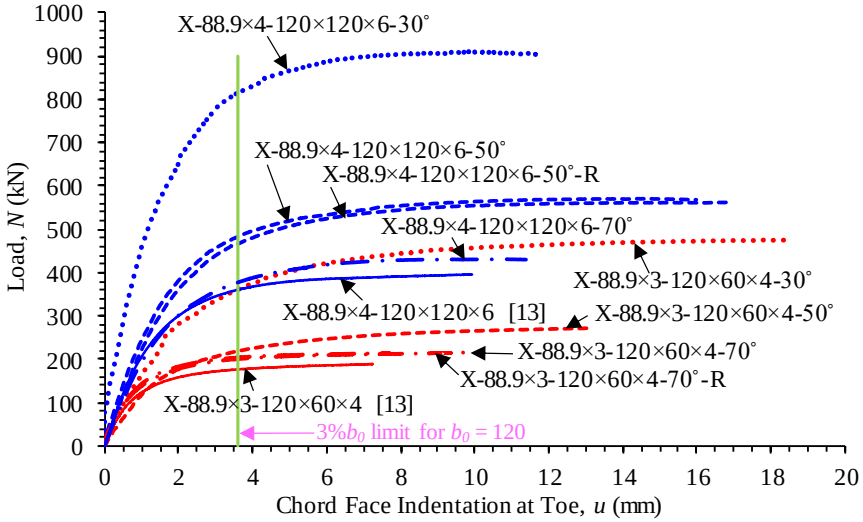

b. Load vs Chord face indentation curves at toe

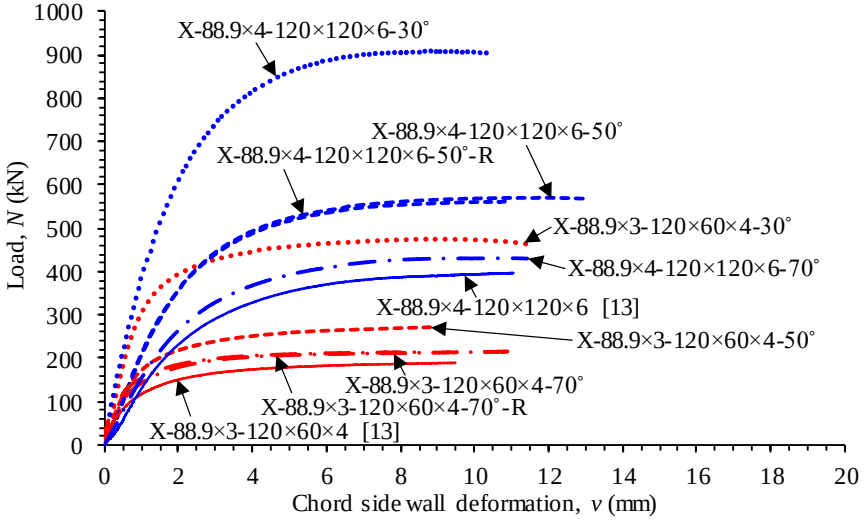

c. Load vs Chord side wall deformation curves

Fig. 21. Load vs deformation curves for CHS-RHS non-90˚ X-joints with chord face failure mode (F)

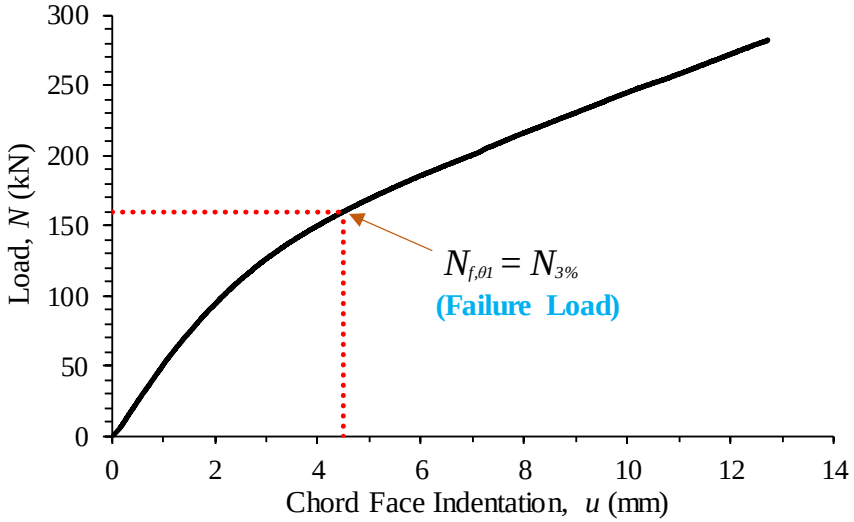

a. For deformation limit criterion ($0.03b_0$ chord face indentation)

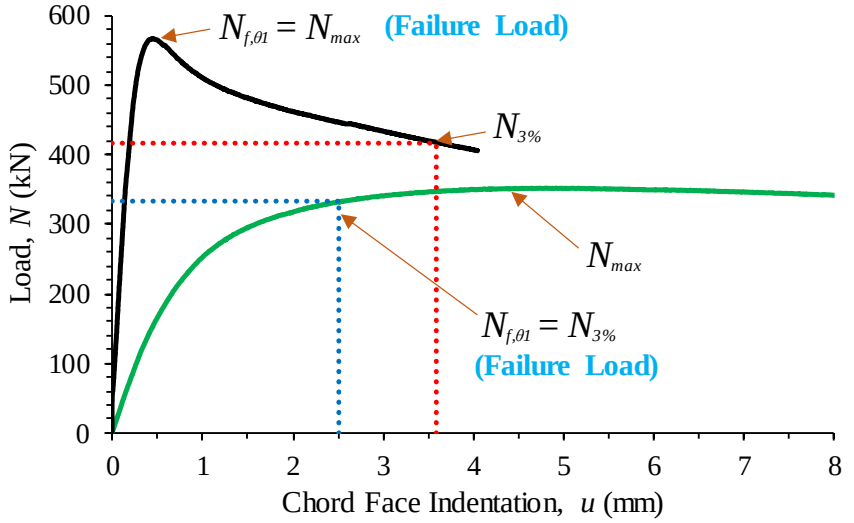

b. For both load and deformation criteria

Fig. 22. Definition of joint failure resistance for load and deformation criteria

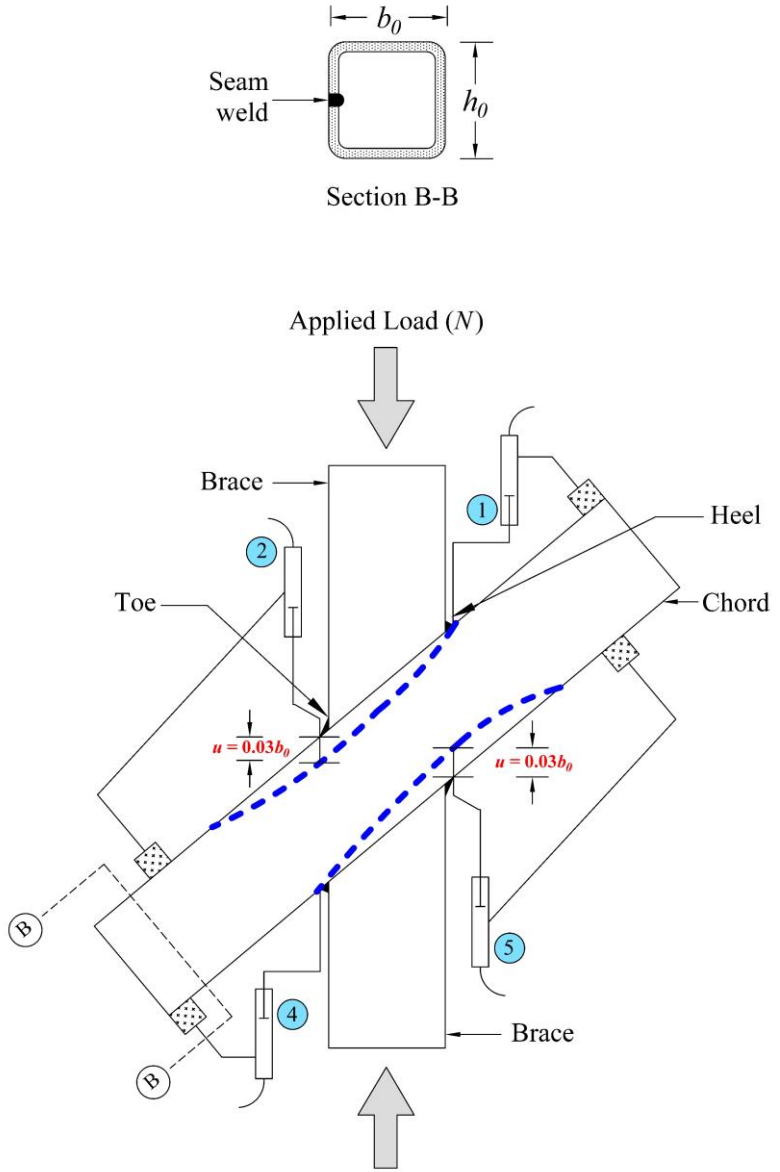

Fig. 23. Relationship between $0.03b_0$ deformation and LVDT

a. RHS-RHS non-90˚ X-joint failed by chord face failure mode (F)

b. RHS-RHS non-90˚ X-joint failed by chord side wall failure mode (S)

c. RHS-RHS non-90˚ X-joint failed by combined failure mode (F+S)

Fig. 24. Observed failure modes of RHS-RHS non-90˚ X-joints

a. Chord face failure mode (F) of X-88.9×4-120×120×6-30°

b. Chord face failure mode (F) of X-88.9×3-120×60×4-70°-R

Fig. 25. Observed failure mode of CHS-RHS non-90˚ X-joints

Specimens	Braces (mm)							Chords (mm)						θ_H	θ_T	Geometric Ratios			
X-b_1×h_1×t_1-b_0×h_0×t_0-θ_1	b_1	h_1	t_1	r_1	R_1	L_H	L_T	b_0	h_0	t_0	r_0	R_0	L_0	(˚C)	(˚C)	β	τ	2γ	h_0/t_0
X-80×80×4-150×150×6-30°	80.2	80.2	3.944	6.6	9.7	160.0	299.5	150.2	151.1	5.893	9.4	12.8	868.6	30.0	149.9	0.53	0.67	25.5	25.6
X-100×100×4-120×60×4-30°	100.8	100.8	3.975	8.3	11.7	200.0	373.2	119.7	61.2	3.956	6.6	9.7	481.8	29.9	150.1	0.84	1.00	30.3	15.5
X-100×100×4-120×60×4-30°-R	100.8	100.8	3.960	8.4	11.7	200.0	373.0	119.9	60.8	3.955	6.6	9.6	483.2	29.9	150.1	0.84	1.00	30.3	15.4
X-120×120×3-140×140×4-30°	120.3	120.0	3.098	4.4	6.7	239.2	448.2	140.3	141.3	4.009	5.6	8.7	899.9	29.8	150.2	0.86	0.77	35.0	35.3
X-120×120×3-120×120×3-30°	120.3	120.1	3.101	4.3	6.7	240.0	448.0	120.2	120.6	3.103	4.4	6.7	808.1	29.8	150.2	1.00	1.00	38.7	38.9
X-120×120×4-120×120×4-30°	121.0	121.2	3.926	6.7	9.9	240.7	447.7	121.5	121.1	3.947	6.7	9.6	806.5	29.7	150.0	1.00	0.99	30.8	30.7
X-80×80×4-150×150×6-50°	80.3	80.2	3.952	6.4	9.6	160.2	226.8	150.1	151.3	5.944	9.2	13.0	678.3	49.9	130.5	0.53	0.66	25.3	25.4
X-120×120×3-150×150×6-50°	120.5	120.0	3.088	4.4	6.8	240.9	340.9	149.9	151.3	5.902	9.1	12.9	709.7	50.0	129.8	0.80	0.52	25.4	25.6
X-100×100×4-120×60×4-50°	100.8	100.8	3.979	8.5	11.9	200.2	284.0	120.0	61.1	3.953	6.5	9.7	361.3	49.6	130.1	0.84	1.01	30.4	15.5
X-120×120×3-140×140×4-50°	120.4	119.9	3.118	4.5	6.9	240.2	341.1	140.0	141.3	3.999	5.6	8.4	691.5	49.8	130.1	0.86	0.78	35.0	35.3
X-120×120×3-120×120×3-50°	120.7	120.0	3.111	4.8	7.2	240.5	340.8	120.2	120.6	3.116	4.4	7.0	615.5	49.7	129.7	1.00	1.00	38.6	38.7
X-120×120×4-120×120×4-50°	120.9	121.2	3.938	6.5	9.5	240.7	341.2	121.5	121.3	3.954	6.6	9.7	615.2	49.7	130.2	1.00	1.00	30.7	30.7
X-80×80×4-150×150×6-70°	80.2	80.0	3.961	6.2	9.3	159.1	188.1	150.1	151.3	5.940	9.1	13.0	588.5	69.7	109.8	0.53	0.67	25.3	25.5
X-120×120×3-150×150×6-70°	120.5	119.9	3.093	4.4	6.7	240.2	283.6	149.9	151.4	5.911	9.2	13.0	604.9	69.8	109.5	0.80	0.52	25.4	25.6
X-100×100×4-120×60×4-70°	101.1	101.0	4.000	8.6	12.5	199.6	235.5	119.9	61.0	3.969	6.4	9.6	308.5	69.0	109.5	0.84	1.01	30.2	15.4
X-120×120×3-140×140×4-70°	120.5	120.0	3.129	4.6	7.0	240.8	283.7	139.9	141.2	4.021	5.4	8.4	597.5	69.6	109.6	0.86	0.78	34.8	35.1
X-120×120×3-120×120×3-70°	120.5	120.0	3.118	4.3	6.5	239.4	283.5	120.3	120.5	3.111	4.4	6.7	530.3	69.6	109.1	1.00	1.00	38.7	38.7
X-120×120×4-120×120×4-70°	120.9	121.1	3.938	6.9	9.7	239.4	284.2	121.8	121.3	3.939	6.8	9.9	530.6	69.5	109.5	1.00	1.00	30.9	30.8

Table 1. Measured average member dimensions for RHS-RHS non-90˚ X-joints

Specimens	Braces (mm)				Chords (mm)						θ_H	θ_T	Geometric Ratios			
X-d_1×t_1-b_0×h_0×t_0-θ_1	d_1	t_1	L_H	L_T	b_0	h_0	t_0	r_0	R_0	L_0	(˚C)	(˚C)	β	τ	2γ	h_0/t_0
X-88.9×3-120×60×4-30°	88.8	3.079	177.6	331.8	119.9	61.3	3.958	6.5	9.6	462.8	30.0	150.1	0.74	0.78	30.3	15.5
X-88.9×4-120×120×6-30°	89.0	3.972	177.8	331.7	122.0	122.0	5.938	7.6	11.7	745.9	30.0	150.0	0.73	0.67	20.6	20.5
X-88.9×3-120×60×4-50°	89.2	2.974	178.8	251.9	119.8	61.0	3.960	6.5	9.6	346.5	49.6	129.9	0.74	0.75	30.2	15.4
X-88.9×4-120×120×6-50°	89.1	3.971	177.4	251.4	122.3	121.9	5.949	7.5	11.8	574.6	49.9	129.6	0.73	0.67	20.6	20.5
X-88.9×4-120×120×6-50°-R	89.2	3.938	177.3	252.4	122.3	121.8	5.965	7.2	12.1	582.0	50.1	129.7	0.73	0.66	20.5	20.4
X-88.9×3-120×60×4-70°	89.0	2.968	177.8	209.9	120.0	61.1	3.958	6.4	9.8	296.7	69.9	109.9	0.74	0.75	30.3	15.4
X-88.9×3-120×60×4-70°-R	89.3	2.967	177.3	210.1	119.9	61.0	3.936	6.3	9.7	296.5	69.4	109.8	0.74	0.75	30.5	15.5
X-88.9×4-120×120×6-70°	89.1	3.950	177.1	210.3	122.2	121.9	5.974	7.3	11.8	496.5	70.0	109.5	0.73	0.66	20.5	20.4

Table 2. Measured average member dimensions for CHS-RHS non-90˚ X-joints

Sections	Nominal	Measured properties				
(b×h×t)	$\sigma_{0.2}$	E_f	$\sigma_{0.2f}$	σ_{uf}	$0.8\sigma_{uf}$	ε_{ff}
	(MPa)	(GPa)	(MPa)	(MPa)	(MPa)	(%)
80×80×4	960	212.2	1003.8	1180.5	944.4	7.91
120×120×3	960	212.0	1038.2	1160.1	928.1	6.63
120×120×4	960	209.4	971.4	1137.9	910.4	7.99
140×140×4	960	208.9	1008.0	1116.4	893.1	7.50
150×150×6	960	208.5	1059.1	1145.7	916.6	9.37
100×100×4	900	207.2	967.0	1092.2	873.8	7.60
120×60×4	900	200.8	910.4	1064.6	851.7	8.03
120×120×6	900	205.6	945.2	1085.5	868.4	9.71

Table 3. Measured material properties obtained from flat regions of tubular members [11]

Sections	Nominal	Measured properties				
(b×h×t)	$\sigma_{0.2}$	E_c	$\sigma_{0.2c}$	σ_{uc}	$0.8\sigma_{uc}$	ε_{fc}
	(MPa)	(GPa)	(MPa)	(MPa)	(MPa)	(%)
80×80×4	960	211.7	1125.6	1249.4	999.5	9.12
120×120×3	960	214.2	1088.2	1211.4	969.1	10.40
120×120×4	960	213.6	1099.5	1231.2	984.9	12.89
140×140×4	960	219.9	1067.9	1180.9	944.7	12.86
150×150×6	960	209.9	1102.4	1233.1	986.5	15.57
100×100×4	900	211.1	1075.9	1147.4	918.0	12.21
120×60×4	900	209.4	1077.2	1145.5	916.4	12.58
120×120×6	900	219.9	1078.1	1149.4	919.5	15.80

Table 4. Measured material properties obtained from corner regions of tubular members [11]

Sections	Nominal	Measured properties				
(d×t)	$\sigma_{0.2}$	E_{cr}	$\sigma_{0.2cr}$	σ_{ucr}	$0.8\sigma_{ucr}$	ε_{fcr}
	(MPa)	(GPa)	(MPa)	(MPa)	(MPa)	(%)
88.9×3	900	206.5	978.6	1097.3	877.9	10.11
88.9×4	900	208.5	1006.7	1105.3	884.3	12.26

Table 5. Measured material properties obtained from curved regions of tubular members [11]

Sections	Nominal	Measured properties		
(b×h×t)	$\sigma_{0.2}$	E_{cp}	$\sigma_{0.2cp}$	$\varepsilon_{0.2cp}$
	(MPa)	(GPa)	(MPa)	(%)
80×80×4	960	220.4	1170.4	0.73
120×120×3	960	222.9	1101.4	0.69
120×120×4	960	212.4	1121.1	0.73
140×140×4	960	217.9	990.8	0.65
150×150×6	960	210.6	1033.2	0.69
100×100×4	900	214.9	1040.6	0.68
120×60×4	900	220.5	1034.6	0.67
120×120×6	900	216.1	1078.2	0.70

Table 6. Measured material properties obtained from compression coupons

Specimens	β	Weld Types	Weld Passes		r_0	R_0	g	G	Side Welds (mm)				Toe Welds (mm)		Heel Welds (mm)	
	(b_1/b_0)		FW	GW	(mm)				w	t_w	w'	w_r	w_0	t_w	w	t_w
X-80×80×4-150×150×6-30°	0.53	FW	1	- - -	9.4	12.8	0	- - -	6.61	4.53	- - -	- - -	10.00	5.00	14.00	11.02
X-100×100×4-120×60×4-30°	0.84	FW	1	- - -	6.6	9.7	0	- - -	7.27	4.46	- - -	- - -	9.61	4.81	12.00	9.09
X-100×100×4-120×60×4-30°-R	0.84	FW	1	- - -	6.6	9.6	0	- - -	7.30	4.60	- - -	- - -	11.18	5.59	12.00	9.21
X-120×120×3-140×140×4-30°	0.86	FW	1	- - -	5.6	8.7	0	- - -	6.76	4.72	- - -	- - -	11.75	5.88	14.21	10.89
X-120×120×3-120×120×3-30°	1.00	FW+GW	1	1	4.4	6.7	0	0.91	- - -	- - -	17.81	3.03	11.50	5.75	17.00	13.92
X-120×120×4-120×120×4-30°	1.00	FW+GW	1	1	6.7	9.6	0	1.54	- - -	- - -	18.96	3.23	11.50	5.75	16.75	13.43
X-80×80×4-150×150×6-50°	0.53	FW	1	- - -	9.2	13.0	0	- - -	6.57	4.60	- - -	- - -	12.75	9.77	9.31	6.34
X-120×120×3-150×150×6-50°	0.80	FW	1	- - -	9.1	12.9	0	- - -	6.34	4.14	- - -	- - -	9.17	7.02	10.93	8.59
X-100×100×4-120×60×4-50°	0.84	FW	1	- - -	6.5	9.7	0	- - -	6.93	3.87	- - -	- - -	9.35	7.16	9.48	7.34
X-120×120×3-140×140×4-50°	0.86	FW	1	- - -	5.6	8.4	0	- - -	6.59	4.30	- - -	- - -	9.78	7.49	10.16	7.31
X-120×120×3-120×120×3-50°	1.00	FW+GW	1	1	4.4	7.0	0	1.00	- - -	- - -	16.55	3.14	7.42	5.68	9.60	7.22
X-120×120×4-120×120×4-50°	1.00	FW+GW	1	1	6.6	9.7	0	1.59	- - -	- - -	19.90	2.52	12.73	9.75	10.00	7.62
X-80×80×4-150×150×6-70°	0.53	FW	1	- - -	9.1	13.0	0	- - -	12.20	8.61	- - -	- - -	11.04	6.52	12.19	9.98
X-120×120×3-150×150×6-70°	0.80	FW	1	- - -	9.2	13.0	0	- - -	8.18	4.78	- - -	- - -	4.79	3.57	7.85	6.34
X-100×100×4-120×60×4-70°	0.84	FW	1	- - -	6.4	9.6	0	- - -	10.69	6.71	- - -	- - -	8.22	4.88	10.24	8.39
X-120×120×3-140×140×4-70°	0.86	FW	1	- - -	5.4	8.4	0	- - -	8.33	4.09	- - -	- - -	6.58	3.98	7.82	6.39
X-120×120×3-120×120×3-70°	1.00	FW+GW	1	1	4.4	6.7	0	0.90	- - -	- - -	15.92	2.75	7.24	4.46	9.16	7.04
X-120×120×4-120×120×4-70°	1.00	FW+GW	1	1	6.8	9.9	0	1.67	- - -	- - -	15.95	3.69	8.15	5.26	8.12	6.30

Note: "- - -" denotes not applicable; FW– Fillet weld; GW – Partial joint penetration flare bevel groove weld.

Table 7. Measured average weld dimensions for RHS-RHS non-90˚ X-joints

Specimens	β (d_1/b_0)	Weld Types	Weld Passes	Side Welds (mm)		Toe Welds (mm)		Heel Welds (mm)	
			FW	w	t_w	w_0	t_w	w	t_w
X-88.9×3-120×60×4-30°	0.74	FW	1	5.82	3.90	7.75	3.88	12.00	9.10
X-88.9×4-120×120×6-30°	0.73	FW	1	6.60	4.48	8.05	4.03	14.50	11.37
X-88.9×3-120×60×4-50°	0.74	FW	1	6.47	4.40	5.92	4.53	5.55	3.72
X-88.9×4-120×120×6-50°	0.73	FW	1	6.72	4.37	11.22	8.60	8.16	6.11
X-88.9×4-120×120×6-50°-R	0.73	FW	1	6.81	4.46	12.72	9.74	9.41	7.11
X-88.9×3-120×60×4-70°	0.74	FW	1	7.91	5.55	6.78	4.37	8.56	7.00
X-88.9×3-120×60×4-70°-R	0.74	FW	1	7.91	5.55	8.64	5.11	7.75	6.07
X-88.9×4-120×120×6-70°	0.73	FW	1	6.01	4.05	6.10	4.01	6.74	5.27

Note: FW– Fillet weld.

Table 8. Measured average weld dimensions for CHS-RHS non-90˚ X-joints

Tubular section thicknesses	Regions	Nominal Strengths	Measured properties			
			E	$\sigma_{0.2}$	σ_u	ε_f
(mm)	(mm)	(MPa)	(GPa)	(MPa)	(MPa)	(%)
3	HAZ - 0 to 6	960	196.3	614.8	724.8	11.99
	HAZ - 6 to 12	960	198.5	873.2	873.9	8.18
	HAZ - 12 to 18	960	205.2	916.5	961.6	9.16
	HAZ - 18 to 24	960	201.9	855.3	1008.6	10.69
	Non-HAZ (Parent Metal)	960	200.6	910.0	1064.6	7.44
4	HAZ - 0 to 6	960	196.6	755.4	835.0	8.03
	HAZ - 6 to 12	960	199.7	881.6	884.7	11.00
	HAZ - 12 to 18	960	232.6	925.4	976.1	4.85
	HAZ - 18 to 24	960	204.6	608.9	1062.0	11.42
	Non-HAZ (Parent Metal)	960	211.8	836.6	1120.5	11.82
6	HAZ - 0 to 6	960	208.4	700.5	974.4	7.29
	HAZ - 6 to 12	960	207.9	1004.1	1003.4	7.25
	HAZ - 12 to 18	960	214.5	901.5	1061.0	6.88
	HAZ - 18 to 24	960	199.2	625.9	1098.1	8.65
	Non-HAZ (Parent Metal)	960	205.0	770.6	1134.1	9.97

Table 9. Measured average material properties from HAZ and Non-HAZ regions

Tubular section thicknesses (mm)	Regions (mm)	Nominal Strengths (MPa)	$\frac{E_{HAZ}}{E}$	$\frac{\sigma_{0.2,HAZ}}{\sigma_{0.2}}$	$\frac{\sigma_{u,HAZ}}{\sigma_{u}}$	$\frac{\varepsilon_{f,HAZ}}{\varepsilon_{f}}$
3	HAZ - 0 to 6	960	0.98	0.68	0.68	1.61
	HAZ - 6 to 12	960	0.99	0.96	0.82	1.10
	HAZ - 12 to 18	960	1.02	1.01	0.90	1.23
	HAZ - 18 to 24	960	1.01	0.94	0.95	1.44
4	HAZ - 0 to 6	960	0.93	0.90	0.75	0.68
	HAZ - 6 to 12	960	0.94	1.05	0.79	0.93
	HAZ - 12 to 18	960	1.10	1.11	0.87	0.41
	HAZ - 18 to 24	960	0.97	0.73	0.95	0.97
6	HAZ - 0 to 6	960	1.02	0.91	0.86	0.73
	HAZ - 6 to 12	960	1.01	1.30	0.88	0.73
	HAZ - 12 to 18	960	1.05	1.17	0.94	0.69
	HAZ - 18 to 24	960	0.97	0.81	0.97	0.87

Table 10. Residual factors for material properties obtained from the HAZ regions

Specimens	β	Test Resistances (kN)				Nominal Resistances (kN)				Resistance Comparisons				
X-b_1×h_1×t_1-b_0×h_0×t_0-θ_1		N_{max}	$N_{3\%}$	$N_{f,\theta 1}$	N_f	$N^*_{E,X}$	$N_{E,X}$	$N^*_{C,X}$	$N_{C,X}$	$\frac{N_{f,\theta 1}}{N^*_{E,X}}$	$\frac{N_{f,\theta 1}}{N_{E,X}}$	$\frac{N_{f,\theta 1}}{N^*_{C,X}}$	$\frac{N_{f,\theta 1}}{N_{C,X}}$	$\frac{N_{f,\theta 1}}{N_f}$
X-80×80×4-150×150×6-30°	0.53	- - -	685.7	685.7	239.4	767.9	614.3	664.6	598.1	0.89	1.12	1.03	1.15	2.86
X-100×100×4-120×60×4-30°	0.84	765.6	763.6	765.6	359.3	898.1	718.5	840.2	756.2	0.85	1.07	0.91	1.01	2.13
X-100×100×4-120×60×4-30°-R	0.84	791.3	789.0	791.3	359.3	892.3	713.8	834.8	751.3	0.89	1.11	0.95	1.05	2.20
X-120×120×3-140×140×4-30°	0.86	777.4	775.9	777.4	310.8	1041.9	833.5	925.1	832.6	0.75	0.93	0.84	0.93	2.50
X-120×120×3-120×120×3-30°	1.00	690.8	690.4	690.8	316.8	72.7	58.2	90.3	81.3	9.50	11.87	7.65	8.50	2.18
X-120×120×4-120×120×4-30°	1.00	1036.9	1034.6	1036.9	566.8	148.9	119.2	185.2	166.7	6.96	8.70	5.60	6.22	1.83
X-80×80×4-150×150×6-50°	0.53	- - -	367.3	367.3	239.4	433.7	346.9	375.3	337.8	0.85	1.06	0.98	1.09	1.53
X-120×120×3-150×150×6-50°	0.80	722.0	718.0	722.0	506.3	947.8	758.2	820.3	738.2	0.76	0.95	0.88	0.98	1.43
X-100×100×4-120×60×4-50°	0.84	475.0	459.7	475.0	359.3	445.8	356.7	417.1	375.4	1.07	1.33	1.14	1.27	1.32
X-120×120×3-140×140×4-50°	0.86	442.6	439.9	442.6	310.8	506.4	405.1	451.4	406.2	0.87	1.09	0.98	1.09	1.42
X-120×120×3-120×120×3-50°	1.00	436.7	400.9	436.7	316.8	73.9	59.1	91.6	82.4	5.91	7.39	4.77	5.30	1.38
X-120×120×4-120×120×4-50°	1.00	763.3	688.3	763.3	566.8	149.4	119.5	185.5	166.9	5.11	6.39	4.12	4.57	1.35
X-80×80×4-150×150×6-70°	0.53	- - -	335.6	335.6	239.4	330.8	264.6	286.3	257.6	1.01	1.27	1.17	1.30	1.40
X-120×120×3-150×150×6-70°	0.80	571.2	567.0	571.2	506.3	698.2	558.6	604.3	543.8	0.82	1.02	0.95	1.05	1.13
X-100×100×4-120×60×4-70°	0.84	403.3	380.5	403.3	359.3	332.1	265.7	310.7	279.6	1.21	1.52	1.30	1.44	1.12
X-120×120×3-140×140×4-70°	0.86	356.8	352.8	356.8	310.8	372.1	297.7	332.7	299.4	0.96	1.20	1.07	1.19	1.15
X-120×120×3-120×120×3-70°	1.00	348.0	- - -	348.0	316.8	73.9	59.1	91.5	82.3	4.71	5.89	3.80	4.23	1.10
X-120×120×4-120×120×4-70°	1.00	613.1	- - -	613.1	566.8	147.8	118.3	183.3	165.0	4.15	5.18	3.34	3.72	1.08
									Mean (P_m)	2.63	3.28	2.30	2.56	1.62
									COV (V_p)	1.033	1.033	0.894	0.894	0.332
									Resistance factor (ϕ)	1.00	1.00	1.00	1.00	- - -
									Reliability index (β_0)	1.24	1.44	1.34	1.44	- - -

Note: "- - -" denotes not applicable; N_f obtained from Pandey and Young [13].

Table 11. Comparison of test resistances with nominal resistances for RHS-RHS non-90˚ X-joints

Parameters	Chord face failure (F)					Combined failure (F+S)					Chord side wall failure (S)				
	$\frac{N_{f,\theta1}}{N^*_{E,X}}$	$\frac{N_{f,\theta1}}{N_{E,X}}$	$\frac{N_{f,\theta1}}{N^*_{C,X}}$	$\frac{N_{f,\theta1}}{N_{C,X}}$	$\frac{N_{f,\theta1}}{N_f}$	$\frac{N_{f,\theta1}}{N^*_{E,X}}$	$\frac{N_{f,\theta1}}{N_{E,X}}$	$\frac{N_{f,\theta1}}{N^*_{C,X}}$	$\frac{N_{f,\theta1}}{N_{C,X}}$	$\frac{N_{f,\theta1}}{N_f}$	$\frac{N_{f,\theta1}}{N^*_{E,X}}$	$\frac{N_{f,\theta1}}{N_{E,X}}$	$\frac{N_{f,\theta1}}{N^*_{C,X}}$	$\frac{N_{f,\theta1}}{N_{C,X}}$	$\frac{N_{f,\theta1}}{N_f}$
No. of Specimens	3	3	3	3	3	9	9	9	9	9	6	6	6	6	6
Mean (P_m)	0.92	1.15	1.06	1.18	1.93	0.91	1.14	1.00	1.11	1.60	6.06	7.57	4.88	5.42	1.49
COV (V_p)	0.094	0.094	0.094	0.094	0.418	0.166	0.166	0.144	0.144	0.331	0.322	0.322	0.321	0.321	0.293
Resistance factor (ϕ)	1.00	1.00	1.00	1.00	- - -	1.00	1.00	1.00	1.00	- - -	1.00	1.00	1.00	1.00	- - -
Reliability index (β_0)	1.15	1.81	1.69	2.00	- - -	1.17	1.86	1.67	2.02	- - -	4.41	4.85	4.08	4.28	- - -

Note: "- - -" denotes not applicable; N_f obtained from Pandey and Young [13].

Table 12. Summarized comparison of test resistances with nominal resistances for RHS-RHS non-90˚ X-joints

Specimens		Test Resistances (kN)				Nominal Resistances (kN)				Resistance Comparisons				
X-d_1×t_1-b_0×h_0×t_0-θ_1	β	N_{max}	$N_{3\%}$	$N_{f,\theta1}$	N_f	$N^*_{E,X}$	$N_{E,X}$	$N^*_{C,X}$	$N_{C,X}$	$\frac{N_{f,\theta1}}{N^*_{E,X}}$	$\frac{N_{f,\theta1}}{N_{E,X}}$	$\frac{N_{f,\theta1}}{N^*_{C,X}}$	$\frac{N_{f,\theta1}}{N_{C,X}}$	$\frac{N_{f,\theta1}}{N_f}$
X-88.9×3-120×60×4-30°	0.74	- - -	361.3	361.3	176.7	432.6	346.1	404.8	364.3	0.84	1.04	0.89	0.99	2.04
X-88.9×4-120×120×6-30°	0.73	910.6	817.7	817.7	361.6	969.4	775.5	890.7	801.6	0.84	1.05	0.92	1.02	2.26
X-88.9×3-120×60×4-50°	0.74	- - -	219.3	219.3	176.7	229.3	183.4	214.5	193.1	0.96	1.20	1.02	1.14	1.24
X-88.9×4-120×120×6-50°	0.73	571.0	486.1	486.1	361.6	505.1	404.1	464.1	417.7	0.96	1.20	1.05	1.16	1.34
X-88.9×4-120×120×6-50°-R	0.73	562.5	469.1	469.1	361.6	507.3	405.9	466.1	419.5	0.92	1.16	1.01	1.12	1.30
X-88.9×3-120×60×4-70°	0.74	- - -	200.3	200.3	176.7	167.0	133.6	156.2	140.6	1.20	1.50	1.28	1.42	1.13
X-88.9×3-120×60×4-70°-R	0.74	- - -	204.1	204.1	176.7	167.5	134.0	156.7	141.0	1.22	1.52	1.30	1.45	1.16
X-88.9×4-120×120×6-70°	0.73	431.6	379.4	379.4	361.6	378.3	302.7	347.6	312.8	1.00	1.25	1.09	1.21	1.05
									Mean (P_m)	0.99	1.24	1.07	1.19	1.44
									COV (V_p)	0.146	0.146	0.142	0.142	0.314
									Resistance factor (ϕ)	1.00	1.00	1.00	1.00	- - -
									Reliability index (β_0)	1.50	2.21	1.88	2.22	- - -

Note: "- - -" denotes not applicable; N_f obtained from Pandey and Young [13].

Table 13. Comparison of test resistances with nominal resistances for CHS-RHS non-90˚ X-joints

Specimens	Geometric Ratios				Failure Modes	At Failure Loads		Governing Deformations (u or v)
X-b_1×h_1×t_1-b_0×h_0×t_0-θ_1	β	τ	2γ	h_0/t_0		u (mm)	v (mm)	
X-80×80×4-150×150×6-30°	0.53	0.67	25.5	25.6	F	4.51	4.70	v
X-100×100×4-120×60×4-30°	0.84	1.00	30.3	15.5	F+S	3.21	2.20	u
X-100×100×4-120×60×4-30°-R	0.84	1.00	30.3	15.4	F+S	3.06	2.53	u
X-120×120×3-140×140×4-30°	0.86	0.77	35.0	35.3	F+S	3.35	9.56	v
X-120×120×3-120×120×3-30°	1.00	1.00	38.7	38.9	S	3.57	8.30	v
X-120×120×4-120×120×4-30°	1.00	0.99	30.8	30.7	S	3.22	5.31	v
X-80×80×4-150×150×6-50°	0.53	0.66	25.3	25.4	F	4.50	5.14	v
X-120×120×3-150×150×6-50°	0.80	0.52	25.4	25.6	F+S	3.44	9.70	v
X-100×100×4-120×60×4-50°	0.84	1.01	30.4	15.5	F+S	1.90	3.02	v
X-120×120×3-140×140×4-50°	0.86	0.78	35.0	35.3	F+S	2.36	12.73	v
X-120×120×3-120×120×3-50°	1.00	1.00	38.6	38.7	S	1.80	6.01	v
X-120×120×4-120×120×4-50°	1.00	1.00	30.7	30.7	S	1.27	4.01	v
X-80×80×4-150×150×6-70°	0.53	0.67	25.3	25.5	F	4.50	6.48	v
X-120×120×3-150×150×6-70°	0.80	0.52	25.4	25.6	F+S	3.77	12.50	v
X-100×100×4-120×60×4-70°	0.84	1.01	30.2	15.4	F+S	1.41	2.42	v
X-120×120×3-140×140×4-70°	0.86	0.78	34.8	35.1	F+S	1.96	13.20	v
X-120×120×3-120×120×3-70°	1.00	1.00	38.7	38.7	S	0.76	4.98	v
X-120×120×4-120×120×4-70°	1.00	1.00	30.9	30.8	S	0.83	3.46	v

Note: F – Chord face failure mode; F+S – Combined failure mode; S – Chord side wall failure mode; u – Chord face indentation; v – Chord side wall deformation.

Table 14. Summary of failure modes for RHS-RHS non-90˚ X-joints

Specimens	Geometric Ratios				Failure Modes	At Failure Loads		Governing Deformations (u or v)
X-d_1×t_1-b_0×h_0×t_0-θ_1	β	τ	2γ	h_0/t_0		u (mm)	v (mm)	
X-88.9×3-120×60×4-30°	0.74	0.78	30.3	15.5	F	3.60	1.48	u
X-88.9×4-120×120×6-30°	0.73	0.67	20.6	20.5	F	3.66	4.02	v
X-88.9×3-120×60×4-50°	0.74	0.75	30.2	15.4	F	3.59	2.03	u
X-88.9×4-120×120×6-50°	0.73	0.67	20.6	20.5	F	3.67	3.80	v
X-88.9×4-120×120×6-50°-R	0.73	0.66	20.5	20.4	F	3.67	3.54	u
X-88.9×3-120×60×4-70°	0.74	0.75	30.3	15.4	F	3.60	3.55	u
X-88.9×3-120×60×4-70°-R	0.74	0.75	30.5	15.5	F	3.60	3.64	v
X-88.9×4-120×120×6-70°	0.73	0.66	20.5	20.4	F	3.67	4.40	v

Note: F – Chord face failure mode; u – Chord face indentation; v – Chord side wall deformation.

Table 15. Summary of failure modes for CHS-RHS non-90˚ X-joints